JOURNAL OF PETROLOGY | VOLUME 0 | NUMBER 0 | PAGES 1–34 | 2010 | doi:10.1093/petrology/egq016
Journal of Petrology Advance Access published May 14, 2010

Crystallization Sequence and Magma Chamber Processes in the Ferrobasaltic Sept Iles Layered Intrusion, Canada

OLIVIER NAMUR[1]*, BERNARD CHARLIER[1], MICHAEL J. TOPLIS[2], MICHAEL D. HIGGINS[3], JEAN-PAUL LIÉGEOIS[4] AND JACQUELINE VANDER AUWERA[1]

[1]DEPARTMENT OF GEOLOGY, UNIVERSITY OF LIÈGE, B-4000, LIÈGE, BELGIUM
[2]DTP-UMR5562, OBSERVATOIRE MIDI-PYRÉNÉES, PAUL SABATIER UNIVERSITY, F-31400, TOULOUSE, FRANCE
[3]SCIENCES DE LA TERRE, UNIVERSITÉ DU QUÉBEC À CHICOUTIMI, G7H 2B1, CHICOUTIMI, QUE., CANADA
[4]ISOTOPE GEOLOGY, ROYAL MUSEUM FOR CENTRAL AFRICA, B-3080 TERVUREN, BELGIUM

RECEIVED SEPTEMBER 13, 2009; ACCEPTED MARCH 16, 2010

The Sept Iles layered intrusion (Quebec, Canada; 564 Ma) is a large plutonic body with a diameter of 80 km and a thickness of 6 km made up from its base to top of a layered series with troctolite and gabbro, and an upper border series with anorthosite, capped by cupolas of A-type granite. Chilled margin compositions suggest a ferrobasaltic parental magma close to that of the Skaergaard intrusion, but much richer in iron and titanium. Samples from drill-cores and surface sampling of the 4·7 km thick layered series reveal a succession of massive troctolites and layered gabbros that contain 24 Fe–Ti oxide layers cm- to m-thick and many anorthositic autolithic blocks. The sequence of crystallization in the layered series is: plagioclase ($An_{72–34}$) and olivine ($Fo_{75–21}$) followed by magnetite and ilmenite, then Ca-rich pyroxene and finally apatite. An olivine gap is observed between Fo_{66} and Fo_{59}. The saturation of Fe–Ti oxides before Ca-rich pyroxene is interpreted to be the result of the high FeO_t and TiO_2 contents and the low CaO content of the parental magma. Contamination by old continental crust has occurred during crystallization of the layered series, as indicated by Sr isotopic compositions ($^{87}Sr/^{86}Sr_{564} = 0·70360–0·70497$). The differentiation trend of the intrusion is interrupted by two large and many small reversals to more primitive compositions of cumulus phases, Cr content of magnetite and lower Sr isotope ratios. These reversals and the intermittent disappearance of some phases are interpreted as resulting from magma chamber replenishments by undifferentiated primitive basaltic magma and mixing with the resident magma.

KEY WORDS: *ferrobasalt; cryptic layering; Fe–Ti oxides; replenishment; fractional crystallization; layered intrusion*

INTRODUCTION

The Sept Iles layered intrusion (Quebec, Canada) is a circular plutonic body (in cross-section) some 80 km in diameter with an estimated volume of 20 000 km^3 (Loncarevic *et al.*, 1990). This huge magmatic event occurred during the later part of the Ediacaran Period (564 Ma, Higgins & van Breemen, 1998) and has significantly contributed to the evolution of the late Precambrian continental crust of Laurentia. It is the third largest layered intrusion in the world, after the Bushveld complex and the Dufek intrusion (Table 1). The Sept Iles intrusion is made up of a troctolitic and gabbroic layered series, an anorthositic upper border series and a broadly granitic upper series (Higgins, 2005). According to Higgins & Doig (1986), all parts of the intrusion are comagmatic and related by a process of fractional crystallization. Together with mafic dykes and the composite Pointe du Criade sill, the Sept Iles layered intrusion is part of the Sept Iles intrusive suite (Higgins, 2005). The rocks of the Sept Iles layered series are dominated by plagioclase, olivine, Fe–Ti oxides, Ca-rich pyroxene and apatite, and thus have strong affinities with the

*Corresponding author. E-mail: onamur@ulg.ac.be

Table 1: Characteristics of some important layered intrusions in the world

Name	Country	Age (Ma)	Area (km^2)	Thickness (km)	Mineralization	Parental magma	Felsic liquids
Bushveld complex[a]	South Africa	2060	65000	7–9	PGE, Cr, V, Fe, Ti, P	High-Mg basaltic andesite and ferrobasalt	Granite
Dufek[b]	Antarctica	182	6600	8–9	PGE	High-Mg basalt	Granophyre
Sept Iles[c]	Canada	564	5000	6	Fe, Ti, P	Ferrobasalt	Granite
Duluth[d]	USA	1100	5000	1–5	PGE, Cu, Ni, Fe, Ti, P, V	Ferrobasalt	Granophyre
Muskox[e]	Canada	1267	4400	1·8	PGE, Cu, Ni, Cr	High-Mg basalt	Granophyre
Stillwater[f]	USA	2700	4400	6·5	PGE, Cu, Ni	Basalt and high-Mg basalt	Granophyre
Great dyke[g]	Zimbabwe	2460	3300	3	PGE, Cu, Ni, Cr	Si- and Mg-rich basalt	–
Windimurra[h]	Australia	2800	2300	13	PGE, V	Al-and Mg-rich basalt	Granophyre
Kiglapait[i]	Canada	1305	560	8·5	Cu, Ni	High-Al basalt	Granophyre
Bjerkreim–Sokndal[j]	Norway	930	230	7·5	Fe, Ti, P, V	Jotunite (ferrobasalt)	Quartz mangerite
Fongen–Hyllingen[k]	Norway	426	160	4·4	–	Basaltic-andesite	Granophyre
Newark Island[l]	Canada	1305	150	>3	Cu, Ni	Ferrobasalt	Granite
Skaergaard[m]	Greenland	55	90	3·5	PGE, Au	Ferrobasalt	Granophyre
Potato River[n]	USA	110	60	3, 6	–	High-Al basalt	Granophyre
Rhum[o]	UK	60	50	1	PGE, Cr	High-Mg basalt	–
Panzhihua[p]	China	263	30	2–3	Fe, Ti, V	Low-Si ferropicrite	–
Fedorivka[q]	Ukraine	1760	3	0·3	Fe, Ti, P, V	Ferrobasalt	

[a]Davies *et al.*, 1980; Davies & Cawthorn, 1984; Kleeman & Twist, 1989; Walraven *et al.*, 1990; Eales & Cawthorn, 1996; Lee, 1996. [b]Himmelberg & Ford, 1977; Beike & Rozgonyi, 1990; Brewer *et al.*, 1996; Ferris *et al.*, 1998. [c]Higgins & Doig, 1986; Loncarevic *et al.*, 1990; Higgins & van Breemen, 1998; Higgins, 2005. [d]Paces & Miller, 1993; Miller & Ripley, 1996. [e]Irvine, 1975; LeCheminant & Heaman, 1989; Day *et al.*, 2008. [f]DePaolo & Wasserburg, 1979; Irvine *et al.*, 1983; Lee, 1996; McCallum, 1996; Meurer & Boudreau, 1996. [g]Bichan, 1970; Hamilton, 1977; Wilson, 1982, 1996; Wilson & Prendergast, 2001. [h]Lee, 1996; Mathison & Ahmat, 1996. [i]Morse, 1969; Morse *et al.*, 1981; DePaolo, 1985; Nolan & Morse, 1986; Blundy, 1997. [j]Duchesne & Hertogen, 1988; Vander Auwera & Longhi, 1994; Schärer *et al.*, 1996; Wilson *et al.*, 1996. [k]Wilson *et al.*, 1983; Wilson & Sorensen, 1996. [l]Simmons *et al.*, 1986; Wiebe, 1988; Wiebe & Snyder, 1993. [m]Hoover, 1989*a*; Hirschmann, 1992; McBirney, 1996; Hirschmann *et al.*, 1997; Nielsen, 2004. [n]Van Schmus *et al.*, 1982; Klewin, 1990. [o]Musset *et al.*, 1988; Emeleus *et al.*, 1996; Butcher *et al.*, 1999. [p]Zhou *et al.*, 2005. [q]Amelin *et al.*, 1994; Duchesne *et al.*, 2006.

ferrogabbros of the Skaergaard intrusion, the Kiglapait intrusion, and the main and upper zones of the Bushveld complex. In this study, we present a detailed petrological investigation of the 4·7 km thick layered series of the intrusion.

Large layered intrusions, such as the Bushveld complex, South Africa (Cawthorn *et al.*, 1991; Mitchell *et al.*, 1998; Kruger, 2005) or the Bjerkreim–Sokndal intrusion, Norway (Nielsen *et al.*, 1996; Wilson *et al.*, 1996), are often characterized by frequent magma chamber replenishments during crystallization, whereas smaller magma bodies such as the Skaergaard intrusion, Greenland (McBirney, 1996) appear to result from the differentiation of a single batch of magma. A detailed study of mineral compositions in the Sept Iles intrusion should therefore contribute to a better understanding of the processes occurring during the filling of large magma chambers.

Preliminary studies of the composition of the chilled margin of the Sept Iles intrusion suggest a ferrobasaltic parent magma (Namur *et al.*, 2007). The sequence of crystallization of ferrobasalt has been investigated in several layered intrusions (e.g. Wager & Brown, 1968; Wiebe, 1988). However, the timing of Fe–Ti oxide saturation is still debated (Juster *et al.*, 1989; Toplis & Carroll, 1995; Jang *et al.*, 2001; Thy *et al.*, 2006, 2009). Additionally, the status of poikilitic Ca-rich pyroxene in the Skaergaard intrusion is not well understood (Holness *et al.*, 2007*a*, 2007*b*). A careful study of mineral modes, textures and compositions in the Sept Iles layered intrusion should contribute to a better understanding of the parameters controlling the relative order of mineral appearance during the crystallization of ferrobasalts.

The geochemical evolution of ferrobasalt magmas during differentiation is a controversial issue, mainly concerning the FeO_t and SiO_2 contents of evolved residual liquids (Byerly *et al.*, 1976; Byerly, 1980; Hunter & Sparks, 1987; Brooks & Nielsen, 1990; McBirney & Naslund, 1990; Morse, 1990; Toplis & Carroll, 1995; Thy *et al.*, 2006, 2009). The most significant unsolved question is: 'Do ferrobasalts evolve to silica-rich A-type granite compositions or to

iron-rich magmas through protracted fractional crystallization?' The Sept Iles layered intrusion has a large massif of A-type granite at the top of the intrusion. The association of A-type granites and igneous layered complexes has been described in many locations (Bonin, 2007). However, except for the Bjerkreim–Sokndal layered intrusion (Duchesne & Wilmart, 1997), large volumes of silicic material have never been described from ferrobasaltic layered intrusions. A detailed study of the Sept Iles liquid line of descent could thus be propitious to highlight the geochemical evolution of ferrobasalts during differentiation.

The Sept Iles layered series is a potential economic resource for Fe, Ti, P and V. It contains 24 layers of practically pure Fe–Ti oxide up to 1 m thick. A 200 m thick layer of apatite-rich gabbro (Critical Zone; Cimon, 1998), in the upper part of the layered series, contains nelsonite layers (magnetite, ilmenite and apatite-rich rocks; Philpotts, 1967; Tollari *et al.*, 2008). The origin of Fe–Ti oxide-rich layers in layered intrusions has been intensively debated, mainly for the Bushveld complex (e.g. Cameron, 1980; Cawthorn & McCarthy, 1980; Kolker, 1982; McCarthy & Cawthorn, 1983; Klemm *et al.*, 1985; Reynolds, 1985; Eales & Cawthorn, 1996; Cawthorn & Ashwal, 2009), but is still poorly understood.

In this study we present a detailed petrographical, mineralogical and geochemical characterization of the Sept Iles layered series based on 216 samples from two drill-cores and surface exposures. New data on mineral and whole-rock compositions as well as Sr-isotopic compositions of plagioclase separates are reported. Our results contribute to a better understanding of the stratigraphy of the intrusion, which constrains the sequence of crystallization, and shed some light on the large-scale magma chamber processes occurring during crystallization of huge volumes of ferrobasaltic magma.

GEOLOGICAL SETTING

Regional geology

The Sept Iles layered intrusion is located on the north shore of the St. Lawrence River, about 500 km NE of Quebec City. It is undeformed and unmetamorphosed and was intruded into high-grade gneisses of the allochthonous polycyclic belt of the Grenville geological province (tectonic events at 1090–980 Ma, affecting Paleo- to Mesoproterozoic lithologies; Davidson, 1984, 1995; Green *et al.*, 1988; Rivers *et al.*, 1989, 1993; Forsyth *et al.*, 1994; Eaton *et al.*, 1995). The Sept Iles intrusion was originally dated at 540 ± 10 Ma (Rb–Sr isochrons; Higgins & Doig, 1977, 1981); a more precise age of 564 ± 4 Ma has subsequently been obtained by U–Pb on zircon (Higgins & van Breemen, 1998). This age is contemporaneous with a widespread magmatic event dominated by basalts, alkaline plutons, kimberlites and carbonatites in eastern Laurentia (Doig & Barton, 1968; Doig, 1970; Kamo *et al.*, 1989; Kumarapeli, 1993; Higgins & van Breemen, 1998). This magmatic event has been attributed to the initiation of the St. Lawrence rift system and the opening of the Iapetus Ocean (Kumarapeli & Saull, 1966; Higgins & van Breemen, 1998). The igneous activity in the Sept Iles area started with the eruption of flood basalts, and the Sept Iles intrusive suite was emplaced between the base of the lavas and the Grenville basement (Higgins, 2005). Hill *et al.* (1992) suggested that this huge magmatic event was related to the activity of a mantle plume. However, we note that the Sept Iles complex is located on a major lithospheric discontinuity, not far from the Grenville Front, during a major ocean opening event, suggesting that it could also result from a lithospheric reorganization process. In either case, the Sr isotopic composition of the Sept Iles intrusion implies a mantle source (Higgins & Doig, 1981).

The Sept Iles layered intrusion

The Sept Iles layered intrusion was first described as a Proterozoic massif-type anorthosite (Wynne-Edwards, 1972; Higgins & Doig, 1977, 1981) because abundant anorthositic rocks crop out in the middle and upper parts of the intrusion. However, geophysical studies by Loncarevic *et al.* (1990) and mapping by Cimon (1998) have revealed a thick sequence of massive troctolites and layered gabbros in the lower part of the intrusion, indicating that Sept Iles would be better interpreted as a mafic layered intrusion (Higgins, 2005).

The intrusion (Fig. 1) has a diameter of 80 km, a maximum thickness of *c.* 6 km and an estimated volume of *c.* 20 000 km^3 (Loncarevic *et al.*, 1990). Layering near the edge of the intrusion dips at 30°, giving an overall shape like a dinner plate. Ninety per cent of its volume is hidden beneath the St. Lawrence River. Only the northern part of the intrusion crops out on the Sept Iles peninsula and on islands from the Sept Iles archipelago. However, thanks to the *c.* 30° dip of the rocks at the margin of the intrusion and the existence of two deep drill-cores (DC-8 and DC-9), a nearly complete stratigraphic section through the layered series is accessible. Five large arcuate magnetic anomalies are observed within the Sept Iles layered intrusion and are interpreted as resulting from the presence of thick Fe–Ti oxide-rich layers (Dion *et al.*, 1998).

The Sept Iles layered intrusion has been divided into three series: the layered series, the upper border series and the upper series (Cimon, 1998; Higgins, 2005). The 4700 m thick layered series, which is the subject of this study, is made up of massive troctolites at the base followed by Fe–Ti oxide-rich troctolites and layered gabbros. The upper border series (less than 1000 m thick) is dominated by anorthosites with minor leucogabbros and

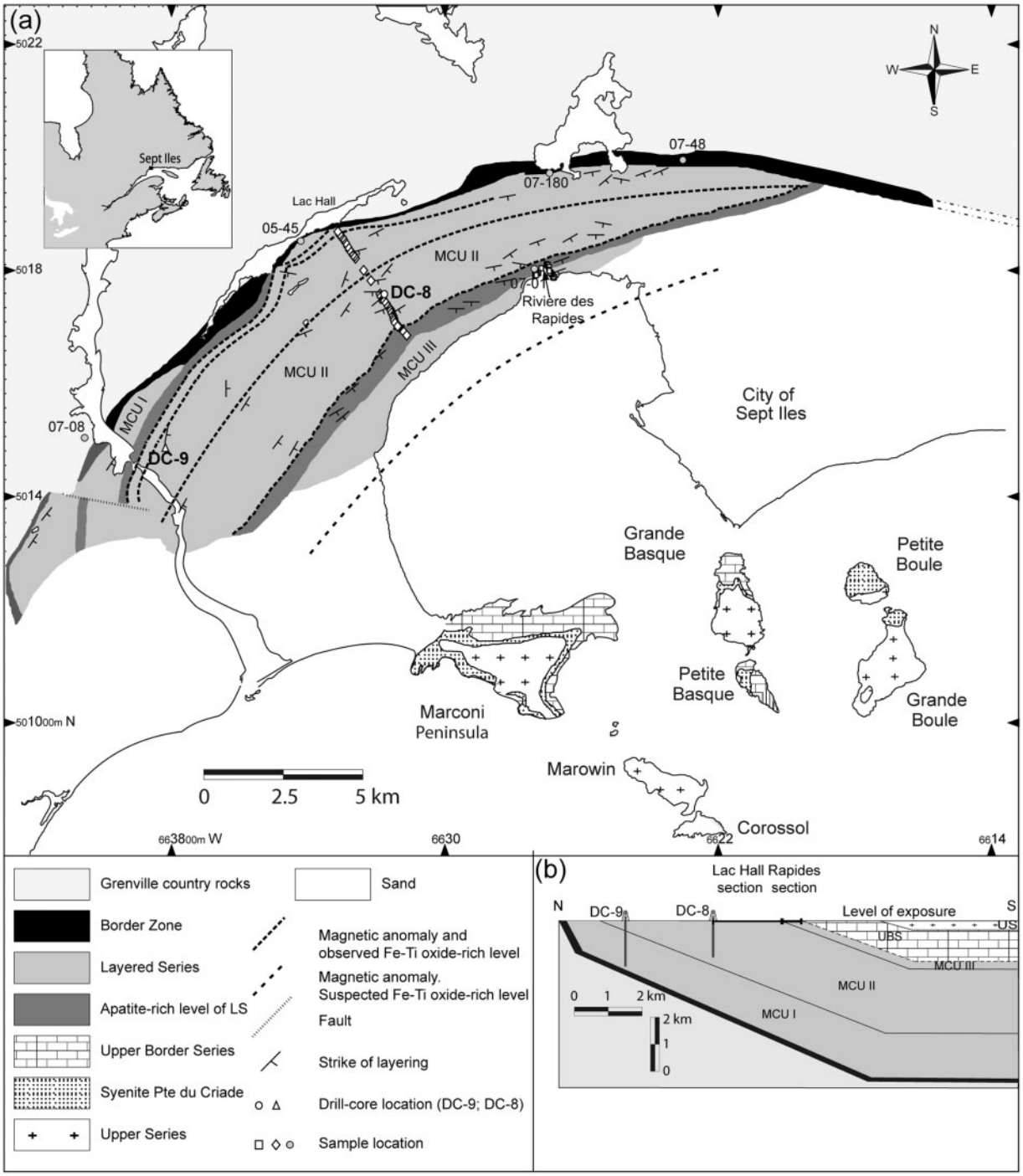

Fig. 1. (a) Geological map of the Sept Iles layered intrusion adapted from Higgins & Doig (1986), Cimon (1998) and Higgins (2005) with subdivision of the layered series into three megacyclic units (MCU). Inset map in the upper left corner shows the location of the map area in the southeastern part of Canada. Locations of surface samples and drill-cores DC-8 and DC-9 are indicated. (b) Schematic cross-section of the Sept Iles layered intrusion indicating the location of the drill-cores and the sections where surface samples were collected. LS, Layered series; UBS, Upper border series; US, Upper series.

leucotroctolites that could have resulted from flotation of plagioclase to the top of the magma chamber (Higgins, 2005). This upper border series contains many centimeter- to decimeter-scale pods of granophyric material, mainly of syenitic and granitic composition. The upper series is made up of A-type granite with minor monzogabbro, monzosyenite, diorite and syenite (Higgins & Doig, 1986). It probably represents less than 10% of the total intrusion and is found only as small separated cupolas.

A thin border of massive fine-grained gabbro is observed in the contact zone between the layered series and the country rocks. The most external part of this border zone commonly displays irregular pods and lenses of evolved material probably resulting from local partial melting of adjacent country rocks. Many centimeter- to meter-scale blocks of country rock are found in the border zone close to the contact (Fig. 2a). Fine-grained gabbros at the contact with the country rocks are traditionally interpreted as chilled margins, representing rapidly cooled magma against the cool country rocks (Wager & Brown, 1968; Hoover, 1989*a*; Naslund, 1989; Cawthorn, 1996).

THE SEPT ILES LAYERED SERIES: FIELD RELATIONSHIPS

From the contact with the border zone to the central part of the layered series, four rock types have been recognized in the field: troctolite, Fe–Ti oxide-rich troctolite, gabbro and apatite-rich gabbro. Troctolite and Fe–Ti oxide-rich troctolite are coarse-grained massive rocks without prominent layering. Gabbroic rocks are finer-grained than troctolites and locally exhibit well-defined layering (Fig. 2b and c), which normally dips 15–30° towards the central part of the intrusion. Igneous layering displays a regular alternation of mafic and more felsic layers. Most layers are generally *c.* 10 cm thick but may range from a few centimeters to more than 1 m. In most mafic layers, the proportion of plagioclase increases upwards, whereas the grain size of minerals decreases. The layering observed in the Sept Iles intrusion is typical of layered igneous complexes and similar features have been described from the Skaergaard intrusion (Wager & Brown, 1968; McBirney & Noyes, 1979; McBirney, 1996), the Panzhihua intrusion (Zhou *et al.*, 2005) and the Fedorivka intrusion (Duchesne *et al.*, 2006). However, it must be noted that layering in the Sept Iles intrusion is much less developed than that described for the Skaergaard intrusion.

In the Sept Iles layered series, Fe–Ti oxide mineralization is concentrated in tabular or lens-shaped massive ore bodies. The latter are frequently responsible for disturbed layering. Tabular ore bodies are represented by centimeter- to meter-thick massive layers (Fig. 2d), with significant lateral extent. They are parallel to the general layering and show sharp lower contacts with the underlying rocks. Upper contacts are more diffuse.

Two 200 m thick layers of apatite-rich gabbro have been recognized in the layered series: one in the middle part and the other in the upper part. The lowermost level is made up of a relatively homogeneous leucocratic gabbro enriched in apatite (~5 wt %). The uppermost level is richer in apatite at its base (up to 30 wt %) and has been named the Critical Zone (Cimon, 1998) because of its potential economic value for phosphorus and titanium. The Critical Zone has a complicated succession in which leucocratic gabbros and Fe–Ti oxide-rich gabbros alternate stratigraphically. Meter-thick nelsonite layers are common in the Critical Zone (Tollari *et al.*, 2008).

Centimeter- to meter-scale angular to rounded anorthositic blocks, called autoliths, are abundant in some parts of the layered series and frequently deform the layering of the underlying rocks (Fig. 2c and e). The textures and the mineralogy of these autoliths are similar to those of anorthosite from the upper border series. Minerals produced by hydrothermal alteration (chlorite, serpentine and epidote) and porosity are found in these rocks. Higgins (2005) thus suggested that they represent blocks from the upper border series, altered by hydrothermal circulation and foundered in the partly solidified layered series. Sonnenthal & McBirney (1998) interpreted the autoliths of the Skaergaard intrusion in a similar way.

Fine- to medium-grained decimeter- to meter-scale mafic and felsic dykes commonly cut the layered series nearly perpendicularly to the layering (Fig. 2f), with sharp contacts. Mafic dykes have textures ranging from porphyric to granular. In the upper part of the layered series, many dykes are composite with mingling relationships between a mafic border and a granitic core.

SAMPLING

Two hundred and sixteen samples were collected from the layered series with a constant spacing of 40 m (Fig. 3). Most of the samples come from two drill-cores (DC-9, 105 samples; DC-8, 54 samples) drilled by Inco Inc., which were made available by the Ministère des Ressources Naturelles et de la Faune du Québec. The reference profile was completed by surface samples collected during the summers of 2005 and 2007 along two cross-sections (Lac Hall section, 33 samples; Rivière des Rapides section, 24 samples). The positions of the surface samples were precisely determined from global positioning system (GPS) coordinates and altimeter data (Fig. 1). One sample (07-08) of country rock was collected at the northern contact of the intrusion. Four samples of fine-grained mafic rocks (05-45, 07-01, 07-48, 07-180) were collected from the Sept Iles border zone and dykes crosscutting the layered series. Their locations are indicated in Fig. 1. The whole-rock compositions of these samples are reported here because,

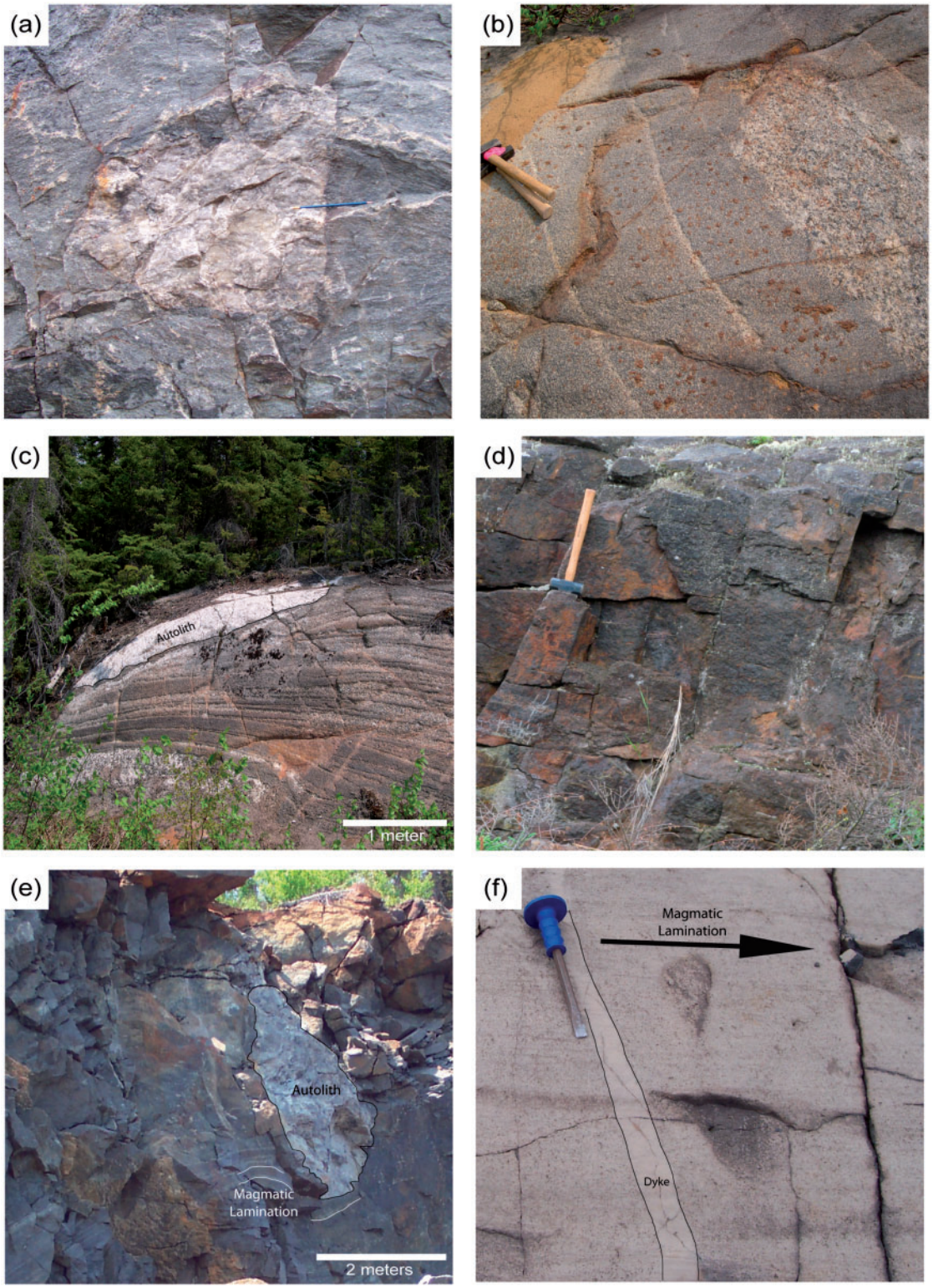

Fig. 2. Photographs of field relations observed in the layered series and in the border zone of the Sept Iles layered intrusion. (a) Quartzite block included within the fine-grained chilled margin of the border zone. (b, c) Centimeter to decimeter rhythmic layering in the Sept Iles layered series, showing alternating plagioclase-rich leucocratic layers and mafic mineral-rich melanocratic layers. A meter-scale autolith (see text) is also observed in (c). (d) Representative outcrop of a meter-scale massive Fe–Ti oxide layer. (e) Anorthositic autolith block in cumulates from the layered series. (Note the deformation of the layering at the base of the autolith, suggesting that the block has foundered into a partially solid crystal pile.) (f) A 10 cm thick dyke of fine-grained gabbro crosscutting cumulates from the upper part of the Sept Iles layered series.

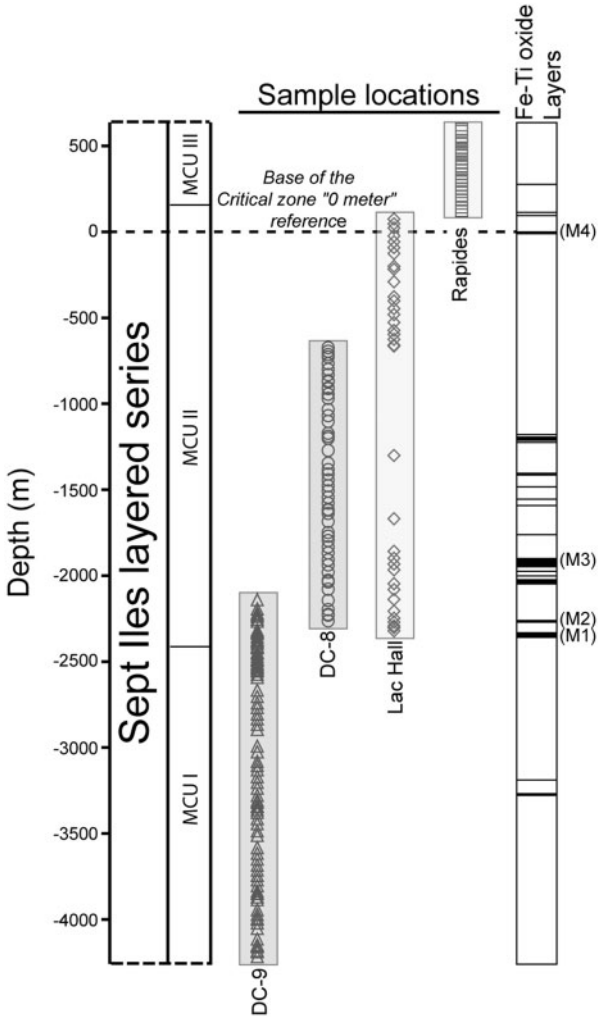

Fig. 3. Schematic cross-section of the Sept Iles layered series showing the total stratigraphic thickness investigated in this study and the subdivision of the layered series into three megacyclic units (MCU I, II and III). Stratigraphic positions of the samples from drill-cores (DC-8 and DC-9) and surface samples are indicated. The right-hand column shows the stratigraphic position of the main Fe–Ti oxide layers. The M2 layer was used to correlate the two drill-cores. M1–M4 are layers inferred to be responsible for the large magnetic anomalies of the Sept Iles layered series (Fig. 2). Lac Hall, Lac Hall section; Rapides, Rivière des Rapides section.

as explained below, they are good candidates to constrain the parental magma composition of the Sept Iles layered intrusion.

The lower part of the layered series does not crop out but is intersected by drill-core DC-9 (Fig. 1b). The lower contact with the country rocks has not been intersected. However, calculations taking into account the typical dip of rocks from the layered series and the length of the DC-9 core suggest that only a small thickness (less than 100 m) of the layered series is missing. The correlation between the two drill-cores is based on a 10 m thick layer of practically pure Fe–Ti oxides (M2; Fig. 3) located at *c.* 160 m in DC-9 and *c.* 1880 m in DC-8. This correlation was confirmed through comparison of mineral compositions. Because the top of the DC-8 bore-hole crops out along the Lac Hall section, correlation between DC-8 and surface samples was achieved by collecting a sample (LHS05-41) close to the top of DC-8 bore-hole. The correlation between the two field sections is based on mineral modes, mineral compositions and stratigraphic reconstruction.

The true stratigraphic position and the distance between samples has been corrected for the average local dip of the igneous layering, estimated at 30° south, drill-cores being vertical. Stratigraphic positions are reported in meters with the '0 meter' reference level chosen as the lowest sample containing apatite in the Critical Zone (Fig. 3). The stratigraphic section investigated in this study is thus 4759 m thick. The upper part of the layered series is located below the St. Lawrence River and it was impossible to estimate precisely the thickness of the missing stratigraphic section. However, it is probably less than 1000 m, because of the low dip of the rocks in the central part of the intrusion (less than 30°).

SUBDIVISION OF THE LAYERED SERIES

One of the most remarkable features of the Sept Iles layered series is the presence of two apatite-rich levels, described by Cimon (1998) and clearly observable in the field (Fig. 1). Where layer types are repeated stratigraphically, the classification of Irvine (1982) suggests subdividing intrusions into different units. The Sept Iles layered series was thus subdivided into three megacyclic units (MCU I, MCU II and MCU III; Figs 1 and 3). As detailed below, mineral compositions, whole-rock geochemistry and Sr isotopic ratios support this subdivision. Each of the first two megacyclic units is topped by a layer of apatite-bearing gabbro. MCU I and MCU II are 1785 m thick and 2553 m thick respectively. MCU III is at least 396 m thick. The upper contact of MCU III is located below the St. Lawrence River and was thus not observed.

PETROGRAPHY

Most of the Sept Iles layered series is made up of equi- to hetero-granular, and medium- to coarse-grained (0·1–25 mm) troctolite and gabbro. Layering is consistent with a cumulate origin of these rocks. Plagioclase, olivine, Ca-rich pyroxene, magnetite, ilmenite and apatite are the most abundant minerals, whereas inverted pigeonite, orthopyroxene, K-feldspar, quartz, biotite, amphibole and Fe–Cu–Ni sulfides (pyrite, chalcopyrite and pyrrhotite) are subordinate.

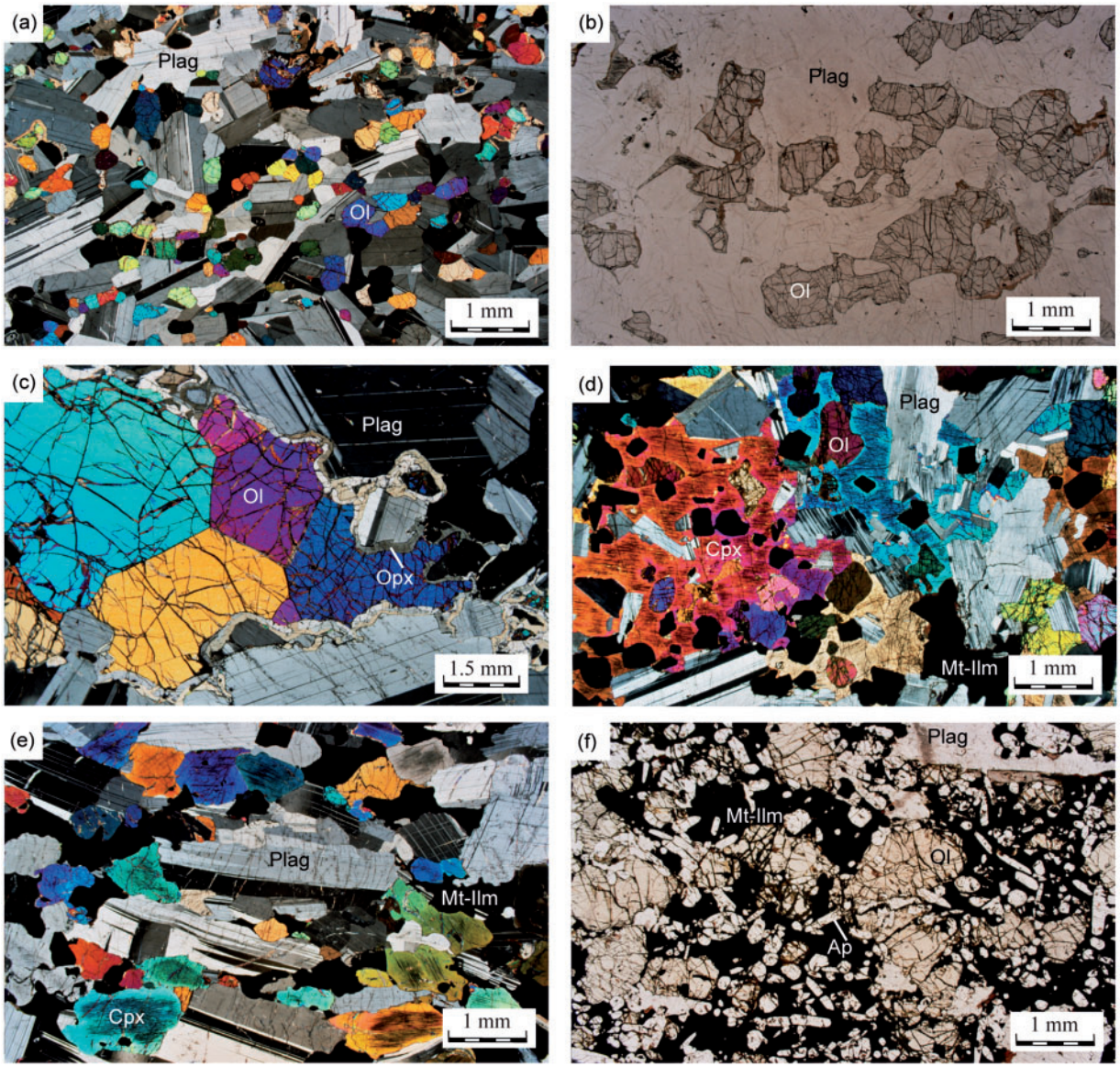

Fig. 4. Photomicrographs showing mineral textures in the Sept Iles layered series. (a) Troctolite with randomly oriented, long lath-shaped plagioclase and millimeter-scale rounded olivine (Sample 9-2267.5; MCU I). (b) Troctolite showing millimeter-scale subhedral to euhedral olivine grains (Sample 9-2373; MCU I). (c) Composite orthopyroxene–amphibole corona around olivine grains with 120° triple junctions (Sample 9-245l; MCU I). (d) Troctolite with large grains of poikilitic Ca-rich pyroxene including small grains of olivine, Fe–Ti oxides and plagioclase (Sample 9-1717.5; MCU I). (e) Foliated gabbro with long lath-shaped plagioclase, tabular Ca-rich pyroxene and millimeter-scale patches of Fe–Ti oxides (Sample 8-31.5; MCU II). (f) Gabbro from the Critical Zone with large subhedral grains of plagioclase and olivine. The matrix of the sample is made up of magnetite and ilmenite and encloses many euhedral grains of apatite (Sample RS 05-07; MCU II). Plag, plagioclase; Mt, magnetite; Ilm, ilmenite; Cpx, Ca-rich pyroxene; Opx, orthopyroxene; Ol, olivine; Ap, apatite.

Plagioclase is a ubiquitous phase with a grain size ranging from 0·1 to 20 mm, in sub-equant to strongly tabular subhedral to euhedral grains (Fig. 4a). In the troctolites from the base of MCU I and the top of MCU III, plagioclase occurs as large grains, randomly oriented and commonly displaying normal or oscillatory zoning. In gabbros from the middle part of MCU I to the lower part of MCU III, plagioclase is unzoned and defines a strong magmatic lamination. Some grains contain abundant needle-shaped Fe–Ti oxide exsolution. Olivine appears as very large (up to 20 mm) subhedral (Fig. 4b) to locally poikilitic grains in troctolites. Contiguous grains commonly have 120° triple junctions (Fig. 4c). In gabbros, olivine has crystallized as small (0·2–4 mm) equant to slightly prismatic

euhedral grains. When prismatic, olivine grains contribute to highlight the magmatic lamination. In samples containing abundant Ca-rich pyroxene, large grains of olivine are uncommon and much of the olivine is frequently represented by 50–200 μm thick coronitic textures around Fe–Ti oxide grains. Calcium-rich pyroxene is represented by very large (5–25 mm) poikilitic grains with irregular shapes in troctolites (Fig. 4d). Oikocrysts enclose many laths of euhedral plagioclase, olivine and locally Fe–Ti oxide grains. The size of the chadacrysts increases towards the margin of the Ca-rich pyroxene grain. In gabbros, Ca-rich pyroxene has crystallized as smaller (up to 5 mm) subhedral to euhedral prismatic grains oriented along the magmatic lamination and frequently twinned (Fig. 4e). Ca-rich pyroxene contains oriented lamellae of Fe–Ti oxides and orthopyroxene probably resulting from exsolution (Hoover, 1989*b*; Morse & Ross, 2004). The cores of Ca-rich pyroxenes also contain many small and regular plates of hematite (Schiller inclusions). Orthopyroxene was observed as coronitic rims around olivine (Fig. 4c) in a few troctolitic samples, as thin lamellae in Ca-rich pyroxene grains and as small anhedral grains. Inverted pigeonite forms subhedral to euhedral prismatic crystals in some rocks of the Critical Zone. Iron–titanium oxide minerals are represented by both the ilmenite–hematite and the magnetite–ulvöspinel solid solutions. In troctolites, oxide minerals occur as small (< 1 mm) patches of anhedral ilmenite with minor magnetite. In Fe–Ti oxide-rich rocks, these minerals crystallize as large grains up to 1 cm, which are frequently polycrystalline and generally dominated by magnetite. Iron–titanium oxide aggregates show an anhedral texture probably resulting from sub-solidus grain boundary migration (Duchesne, 1999). Euhedral Fe–Ti oxide grains have locally been observed as inclusions in silicate minerals. Many Fe–Ti oxide grains are rimmed by brown amphibole and biotite. Apatite is an accessory phase in most of the layered series, where it crystallizes as small (*c.* 50 μm) needles located in the rim of silicate phases or in interstices between them. In two 200 m thick layers, apatite is found as euhedral millimeter-sized grains (Fig. 4f).

LITHOLOGICAL STRATIGRAPHY AND MINERAL COMPOSITION

The Sept Iles stratigraphy has been investigated using a continuous series of samples from the two drill-cores (DC-8 and DC-9), the upper part of the Lac Hall section and the Rivière des Rapides section. Samples from the lower part of the Lac Hall section were not used as they come from a stratigraphic interval that is also intersected by DC-8.

The lower part of MCU I (from −4200 to −3600 m) is made up of plagioclase (*c.* 70 wt %) and olivine (20–30 wt %) cumulates, with minor Ca-rich pyroxene and Fe–Ti oxides (Figs 5a and 6; see Supplementary Dataset 1, available for downloading at http://www.petrology.oxfordjournals.org). Plagioclase and olivine are the cumulus phases (po-C cumulates; Irvine, 1982) and their mineral proportions closely mimic the cotectic proportions found in ferrobasaltic melting experiments (plagioclase 73%, olivine 27%) by Snyder *et al.* (1993), Toplis & Carroll (1995) and Thy *et al.* (2006). The modal proportions of Fe–Ti oxides increase progressively from −3600 to −3400 m reaching *c.* 15 wt % magnetite and *c.* 10 wt % ilmenite (pomi-C cumulates; Figs 5b and 6), whereas the modal proportion of Ca-rich pyroxene increases abruptly at −3500 m to reach values greater than 30 wt % (pomic-C cumulates; Figs 5c and 6). A similar proportion of Ca-rich pyroxene was found in experiments on ferrobasalts (clinopyroxene: 25–40%; Toplis & Carroll, 1995). In the interval between −3000 and −2600 m, the modal proportion of olivine decreases considerably and is frequently less than 5 wt %, indicating an intercumulus status for olivine in this interval (pmic-C cumulates; Figs 5d and 6). Apatite is a cumulus phase in the upper 200 m of MCU I (pomica-C cumulates; Fig. 6). The base of MCU I is marked by a 60 m thick marginal reversal (Fig. 7) in the composition of plagioclase ($An_{63–68}$; Table 2; Supplementary Dataset 2), olivine ($Fo_{68–72}$; Table 3; Supplementary Dataset 3) and Ca-rich pyroxene (Mg-number 76–79; Table 4; Supplementary Dataset 4). This up-section increase of An, Fo and cpx Mg-number is followed by a continuous decrease of these parameters to the top of MCU I, where they reach An_{47}, Fo_{55} and cpx Mg-number 68. The rate of decrease of An%, Fo% and cpx Mg-number % increases significantly in the upper part of MCU I. Orthopyroxene (Table 4; Supplementary Dataset 5) shows a compositional evolution similar to that of olivine and Ca-rich pyroxene. The concentrations of Sr and Ba in plagioclase are relatively constant in the first 1300 m of MCU I, before increasing significantly at the top of MCU I (Fig. 8). The Te content [tephroite; $Te = 100Mn/(Mg + Fe + Mn)$] of olivine is constant until the last 300 m of MCU I, whereas the Jo content [johannsenite; $Jo = 100Mn/(Mg + Fe + Mn)$] of Ca-rich pyroxene increases continuously throughout MCU I. The Cr content of magnetite increases from the base of MCU I to −3600 m, before dropping to below the detection limit at the top of MCU I (Table 5; Supplementary Dataset 6).

In MCU II, plagioclase has a high modal proportion, mainly between 40 and 50 wt %, and is always a cumulus phase (Fig. 6). The olivine mode displays large sample-to-sample variations. It is relatively high in the lower part of MCU II and then decreases upwards. A very low modal proportion of olivine is observed in two intervals, from −900 to −700 m and from −400 m

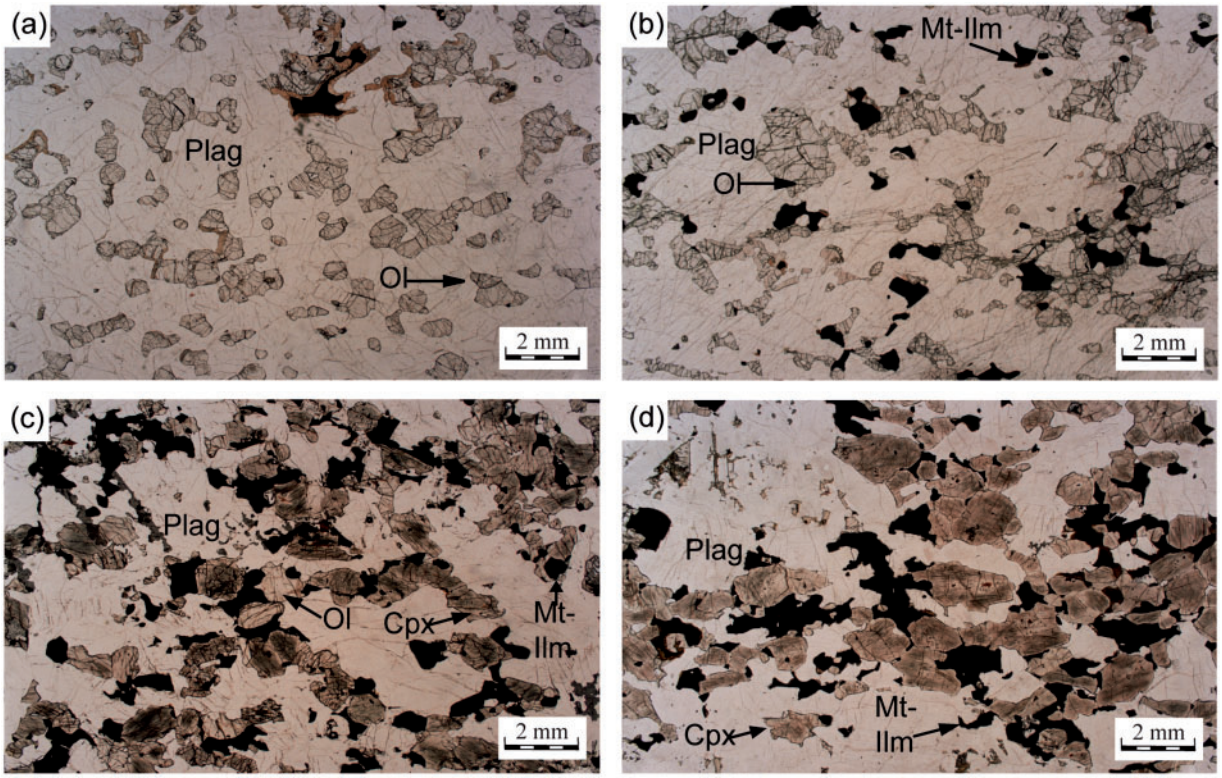

Fig. 5. Photomicrographs showing the cumulus assemblages observed in rocks from the Sept Iles layered series. (a) Troctolite (po-C) containing small rounded grains of cumulus olivine, large lath-shaped grains of plagioclase and minor intercumulus Fe–Ti oxides (Sample 9-2267.5; MCU I). (b) Massive Fe–Ti oxide troctolite (pomi-C) containing large rounded grains of olivine, plagioclase and millimeter-scale anhedral patches of Fe–Ti oxides (Sample 8-1309; MCU II). (c) Gabbro (pomic-C) containing abundant tabular Ca-rich pyroxene. Ca-rich pyroxene and plagioclase together display a well defined-magmatic lamination (Sample 9-1261.5; MCU I). (d) Gabbro (pmic-C) containing abundant Ca-rich pyroxene, plagioclase and Fe–Ti oxides. The disappearance of primary olivine grains should be noted (Sample 8-31.5; MCU II). Cumulus assemblages following the nomenclature of Irvine (1982). Mineral abbreviations in cumulus assemblages: p, plagioclase; o, olivine; m, magnetite; i, ilmenite; c, Ca-rich pyroxene; a, apatite; -C, cumulus. Abbreviations as in Fig. 4.

to −50 m. Olivine is interpreted as an intercumulus phase in these two intervals. The modal proportion of Ca-rich pyroxene is highly variable in the first 1300 m of MCU II, where the status of this mineral alternates between being a cumulus and intercumulus phase on a scale of *c.* 100 m. The Ca-rich pyroxene mode then becomes more constant and relatively high (*c.* 30 wt %) until the top of MCU II. The mode of iron–titanium oxides also displays large variations from sample to sample in MCU II but, except in a few cases, their cumulative proportions are always higher than 10 wt %. Magnetite and ilmenite are thus considered as cumulus phases throughout MCU II. Cumulus apatite occurs in the last 200 m of MCU II (Critical Zone). MCU II starts with a rapid upwards increase in the An content of plagioclase (from An_{47} to An_{62}), the Fo content of olivine (from Fo_{55} to Fo_{70}) and the Mg-number of Ca-rich pyroxene (from 68 to 74; Fig. 7). Relatively constant compositions of plagioclase (*c.* An_{62}), olivine (*c.* Fo_{70}) and Ca-rich pyroxene (*c.* Mg-number 72) are then observed until −1045 m. In detail, this latter 1300 m thick stratigraphic interval is characterized by many significant reversals occurring on a scale of 25–120 m and in the range of 1–4% An, 1–3% Fo and 1–3% cpx Mg-number. From −1045 to −680 m, An%, Fo% and cpx Mg-number decrease continuously from An_{62} to An_{54}, Fo_{70} to Fo_{62} and 74 to 72 before displaying a significant reversal up to An_{58}, Fo_{67} and 75 at −590 m. The compositions of plagioclase, olivine and Ca-rich pyroxene then rapidly evolve to An_{34}, Fo_{21} and cpx Mg-number 55 at the top of MCU II. Orthopyroxene was observed only as subordinate intercumulus grains and displays a compositional evolution similar to the other ferro-magnesian silicates. Potassic feldspar is a subordinate phase in the upper part of MCU II and its orthoclase content increases upwards from 62 to 89 (Table 6). Minor and trace elements in plagioclase (Sr, Ba), olivine (Mn: Te%) and Ca-rich pyroxene (Mn: Jo%) show evolutionary trends opposite to those of An%, Fo% and cpx Mg-number % (Fig. 8). They are relatively

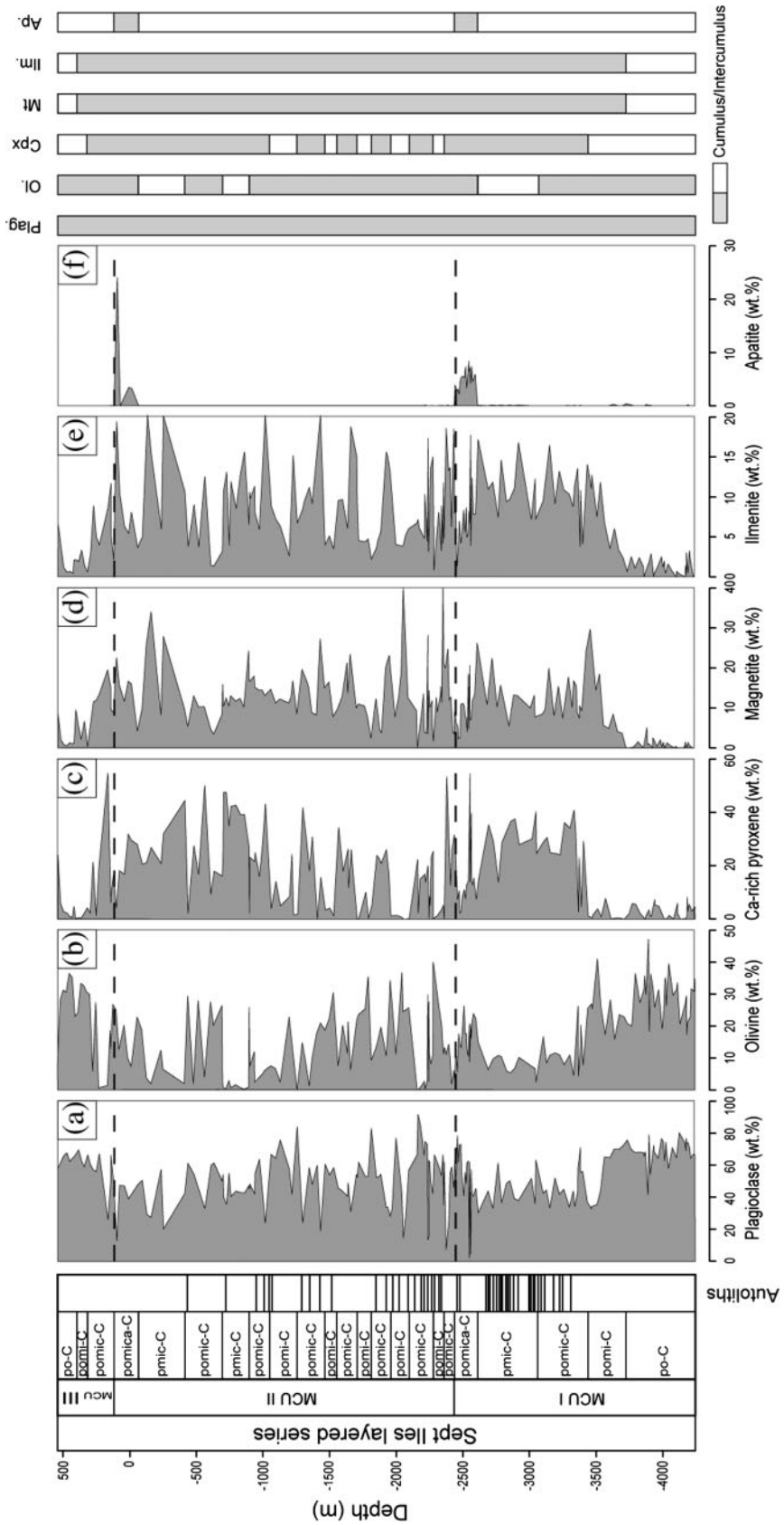

Fig. 6. Mineral modes (see Appendix) of (a) plagioclase, (b) olivine, (c) Ca-rich pyroxene, (d) magnetite, (e) ilmenite and (f) apatite in the Sept Iles layered series and stratigraphy of cumulus (grey) and intercumulus (white) phases in the Sept Iles layered series. The stratigraphic distribution of autoliths is indicated. Dashed lines represent the boundaries between the MCU.

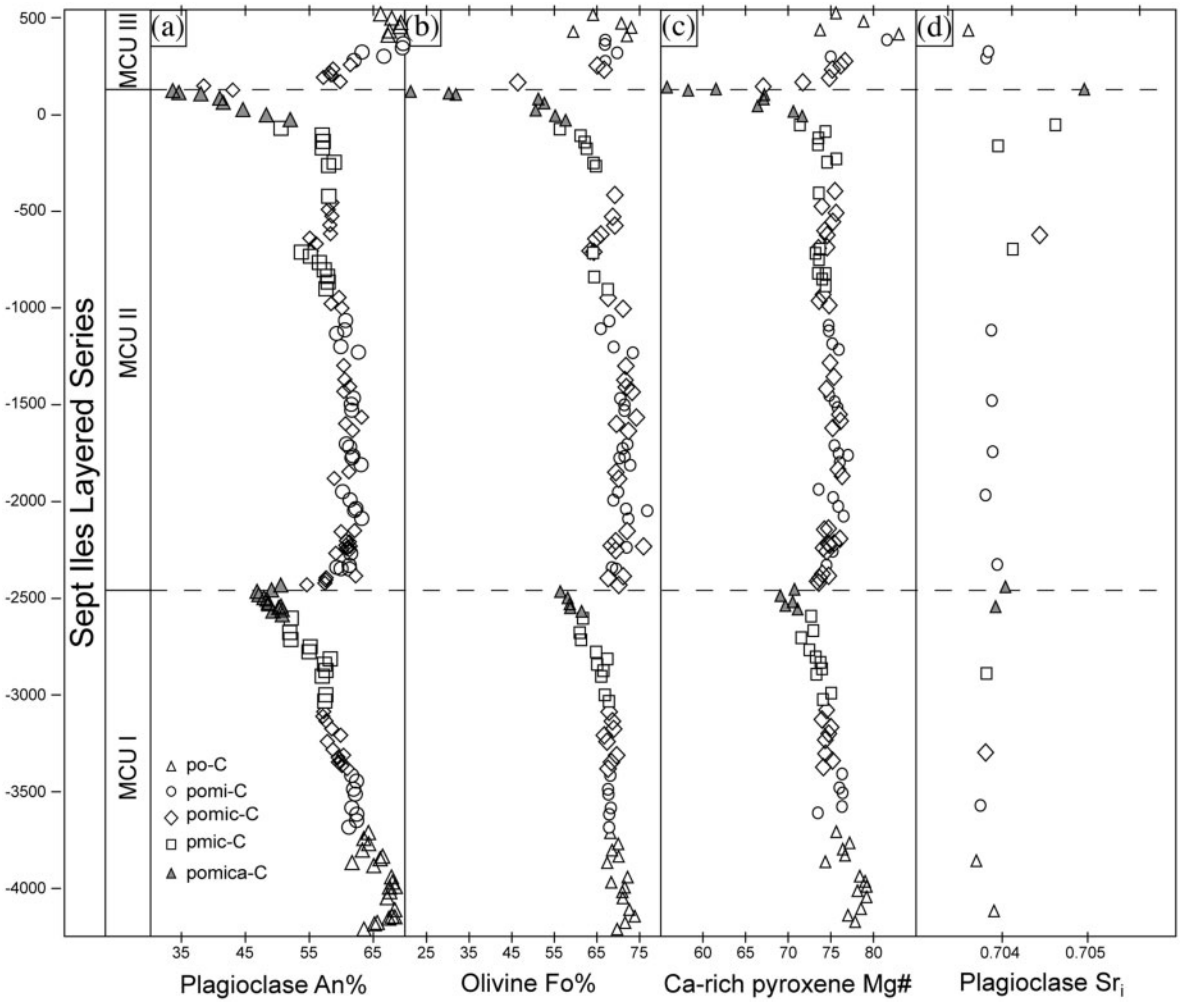

Fig. 7. Major element compositional variation of (a) plagioclase (An%), (b) olivine (Fo%), (c) Ca-rich pyroxene (Mg-number) with stratigraphic position in the Sept Iles layered series. (d) $(^{87}Sr/^{86}Sr)_{564}$ variation in plagioclase separates. Dashed lines represent boundaries between MCU.

constant or slightly increase in the lower part of MCU II to −680 m before reversing to slightly lower concentrations (from −680 to −590 m). In the upper part of MCU II, their concentrations increase to reach the highest values of the layered series. In MCU II, the Cr content of magnetite displays a complex succession of small cycles occurring on a scale of 200–400 m. Each cycle starts with an increase in the magnetite Cr content, reaching concentrations higher than 1000 ppm, and is followed by an abrupt decrease to less than 100 ppm. In the last 300 m of MCU II, cyclicity ends and the magnetite Cr content drops below the detection limit.

In MCU III, Ca-rich pyroxene becomes a minor component and thus the cumulates are made up of Fe–Ti oxide-rich troctolite and troctolite similar to those observed at the base of MCU I (Fig. 6). Throughout MCU III, the compositions of the silicate minerals show a significant progressive reversal to An_{70}, Fo_{70} and cpx Mg-number 73 (Fig. 7). The magnetite Cr content increases to 29–000 ppm, whereas the minor and trace element concentrations of plagioclase, olivine and Ca-rich pyroxene decrease continuously throughout MCU III (Fig. 8).

The major element compositions of magnetite and ilmenite do not display any systematic variation with stratigraphy, except for the MgO content of ilmenite, which decreases upwards in each MCU (Table 7). The TiO_2 content of magnetite ranges from 4·78 to 16·48 wt %, corresponding to recalculated ulvöspinel contents from 0·14 to 0·49 (Table 5). Ilmenite displays ranges of MgO from 0·63 to 3·61 wt % and Fe_2O_3 from 3·89 to 8·89 wt %, corresponding to recalculated hematite proportions varying

Table 2: Representative major (wt %) and trace (ppm) element compositions of separated plagioclase from the Sept Iles layered series [X-ray fluorescence (XRF) analyses]

Sample no.	MCU	Cumulus assemblage	Height (m)	SiO_2	TiO_2	Al_2O_3	FeO_t	MgO	CaO	Na_2O	K_2O	Total	An	Or	Sr	Ba
9-2533.5	I	po-C	−4210	51·68	0·08	30·29	0·44	0·17	12·71	4·07	0·23	99·67	63·3	1·4	1040	181
9-2451	I	po-C	−4142	51·35	0·08	30·29	0·54	0·23	13·28	3·52	0·24	99·54	67·6	1·4	1024	135
9-2111.5	I	po-C	−3864	51·88	0·09	29·92	0·43	0·15	12·52	4·33	0·21	99·53	61·5	1·2	1051	137
9-1886.5	I	pomi-C	−3680	52·46	0·09	29·36	0·42	0·14	12·21	4·31	0·21	99·20	61·0	1·2	1069	153
9-1514.5	I	pomic-C	−3375	52·39	0·08	29·91	0·37	0·10	12·42	4·43	0·23	99·93	60·8	1·3	1050	164
9-772.5	I	pmic-C	−2767	54·02	0·08	28·81	0·35	0·07	11·25	5·09	0·28	99·95	55·0	1·6	1262	235
9-514	I	pomica-C	−2556	54·75	0·09	27·72	0·34	0·07	10·13	5·71	0·35	99·16	49·5	2·0	1474	514
9-389	I	pomica-C	−2453	55·92	0·09	27·55	0·55	0·13	9·62	5·97	0·34	100·17	47·1	1·9	1620	554
9-245	II	pomi-C	−2335	52·99	0·10	29·69	0·43	0·17	12·13	4·50	0·31	100·32	59·8	1·8	1142	228
8-1917.5	II	pomi-C	−2255	52·14	0·07	30·28	0·46	0·16	12·29	4·29	0·12	100·23	61·3	0·7	1085	232
8-1633.5	II	pomi-C	−2023	52·28	0·08	30·18	0·36	0·16	12·75	4·30	0·22	100·35	62·1	1·3	1075	209
8-1264	II	pomi-C	−1700	52·61	0·09	29·98	0·43	0·18	12·45	4·38	0·23	100·34	61·1	1·3	1087	211
8-814	II	pomic-C	−1352	52·51	0·08	29·77	0·46	0·18	12·37	4·49	0·21	100·10	60·4	1·2	1065	213
8-118	II	pmic-C	−782	53·45	0·08	29·25	0·40	0·13	11·78	4·85	0·20	100·17	57·3	1·2	1110	241
8-5.5	II	pmic-C	−690	54·01	0·09	28·47	0·50	0·17	10·98	5·21	0·27	99·72	53·8	1·6	1186	318
LHS 05-40	II	pomic-C	−680	53·35	0·07	28·79	0·56	0·18	11·27	5·09	0·22	99·54	55·0	1·3	1078	307
LHS 07-152	II	pmic-C	−222	52·64	0·07	29·63	0·60	0·16	11·86	4·59	0·10	99·65	58·8	0·6	1118	246
LHS 07-158	II	pomica-C	0	54·77	0·05	28·22	0·43	0·16	10·60	5·38	0·29	99·90	52·1	1·7	1253	349
LHS 07-159	II	pomica-C	52	56·49	0·06	26·80	0·43	0·22	9·07	6·13	0·51	99·72	45·0	2·9	1167	611
RS 05-53	II	pomica-C	134	59·01	0·05	24·92	0·33	0·10	7·25	6·37	0·87	98·90	38·6	5·2	1631	676
RS 07-120	II	pomica-C	150	59·80	0·03	25·23	0·21	0·01	7·05	7·45	0·19	99·96	34·3	1·1		
RS 07-73	III	pomi-C	351	51·82	0·06	30·36	0·44	0·19	11·93	3·87	0·66	99·32	63·0	4·0	1108	112
RS 07-77	III	pomi-C	395	51·48	0·05	30·67	0·51	0·18	12·56	3·08	0·24	98·77	69·3	1·6	1148	127
RS 07-87	III	po-C	439	50·51	0·06	30·87	0·43	0·13	13·42	3·66	0·17	99·25	67·0	1·0	1101	136
RS 07-88	III	po-C	461	51·04	0·06	30·62	0·45	0·14	13·22	3·57	0·31	99·41	67·2	1·8	1045	114

$An = 100[Ca/(Ca + Na)]$; $Or = 100[K/(Ca + Na + K)]$.

from 0·03 to 0·08. In most of the layered series, Fe–Ti oxide minerals occur as disseminated grains in a matrix of silicate minerals. However, they are locally concentrated in practically pure Fe–Ti oxide layers. Twenty-four Fe–Ti oxide layers have been recognized through careful examination of the drill-cores and surface samples. Most of them are centimeters to decimeters thick but two layers are thicker than 10 m (Table 8). The 19 thicker layers are shown in Fig. 3. In samples containing abundant Fe–Ti oxides, these minerals re-equilibrate strongly with the ferromagnesian minerals, mainly olivine, which become richer in MgO.

The stratigraphic position of autoliths (anorthosite blocks that have foundered into the crystal pile of the layered series) is shown in Fig. 6. It is worth noting that autoliths are absent in the first 900 m of the layered series and are uncommon in the uppermost 700 m. Furthermore, autoliths are observed only above the stratigraphic level at which Fe–Ti oxides are cumulus phases (Fig. 6).

WHOLE-ROCK COMPOSITIONS

Sept Iles whole-rock samples are fresh when observed under the microscope and as indicated by their low loss-on-ignition (LOI) values (Supplementary Dataset 7). They display large variations in modal mineralogy (Fig. 6), which are reflected in their whole-rock compositions. Modal mineralogy suggests a stratigraphic succession of different cumulus assemblages in the layered series. The average whole-rock compositions of these assemblages are given in Table 9 and represented in Fig. 9. From po-C to pomica-C cumulate types, the increasing proportion of Fe–Ti oxides and Ca-rich pyroxene is underlined by an increase in the FeO_t and TiO_2 whole-rock contents, and the decreasing proportion of plagioclase is reflected in the decreasing Al_2O_3 and SiO_2 contents of the whole-rocks. The whole-rock MgO and Na_2O contents decrease and increase respectively from po-C to pomica-C, probably reflecting the changing mineral compositions. CaO does not

Table 3: Representative microprobe analyses of olivine from the Sept Iles layered series

Sample no.	*n*	MCU	Cumulus assemblage	Height (m)	SiO_2	TiO_2	Al_2O_3	FeO_t	MnO	MgO	CaO	Na_2O	K_2O	Total	Fo	Te
9-2533.5	7	I	po-C	−4210	37·33	0·02	0·03	28·05	0·40	33·79	0·05	0·02	0·01	99·69	68·2	0·46
9-2451	11	I	po-C	−4142	37·28	0·03	0·03	25·07	0·40	36·60	0·16	0·02	0·01	99·60	72·2	0·45
9-2111.5	6	I	po-C	−3864	36·96	0·02	0·03	29·77	0·43	32·36	0·05	0·02	0·02	99·65	66·0	0·50
9-1886.5	13	I	pomi-C	−3680	37·43	0·02	0·02	29·28	0·45	32·45	0·07	0·02	0·01	99·76	66·4	0·52
9-1514.5	11	I	pomic-C	−3375	37·38	0·03	0·03	29·60	0·41	32·45	0·04	0·02	0·01	99·96	66·2	0·47
9-772.5	13	I	pmic-C	−2767	36·79	0·04	0·02	31·74	0·50	30·89	0·06	0·01	0·01	100·06	63·4	0·58
9-514	12	I	pomica-C	−2556	36·32	0·03	0·03	34·07	0·61	28·81	0·07	0·03	0·01	99·99	60·1	0·72
9-389	7	I	pomica-C	−2453	36·13	0·03	0·02	37·39	0·58	25·32	0·07	0·01	0·01	99·55	55·3	0·70
9-245	24	II	pomi-C	−2335	37·36	0·04	0·03	28·22	0·50	33·62	0·13	0·02	0·01	99·93	68·0	0·57
8-1633.5	22	II	pomi-C	−2023	37·40	0·04	0·03	26·38	0·39	34·96	0·05	0·01	0·02	99·29	70·3	0·44
8-1264	13	II	pomi-C	−1700	37·42	0·03	0·03	26·92	0·41	34·39	0·08	0·02	0·01	99·32	69·5	0·46
8-118	9	II	pomi-C	−782	36·72	0·06	0·04	32·17	0·54	30·67	0·04	0·01	0·00	100·25	63·0	0·46
8-5.5	4	II	pomi-C	−690	36·46	0·03	0·02	32·31	0·61	30·48	0·05	0·01	0·01	99·99	62·7	0·71
LHS 07-40	16	II	pomic-C	−2309	37·48	0·03	0·02	27·24	0·42	34·54	0·07	0·01	0·01	99·83	69·3	0·48
LHS 07-152	12	II	pmic-C	−222	36·55	0·02	0·02	32·32	0·53	30·68	0·05	0·01	0·00	100·22	62·9	0·61
LHS 07-158	13	II	pomica-C	0	35·77	0·03	0·02	36·83	0·67	26·80	0·05	0·01	0·01	100·19	56·5	0·80
LHS 07-159	7	II	pomica-C	52	34·68	0·03	0·02	41·67	0·77	23·04	0·04	0·02	0·01	100·40	49·6	0·93
RS 07-120	13	II	pomica-C	150	31·30	0·02	0·01	58·01	1·40	8·72	0·06	0·01	0·00	99·53	21·1	1·89
RS 07-73	9	III	pomi-C	351	36·86	0·02	0·03	28·34	0·36	34·14	0·02	0·01	0·01	99·92	68·2	0·40
RS 07-77	16	III	pomi-C	395	36·93	0·03	0·12	30·12	0·36	31·99	0·10	0·03	0·01	99·81	65·4	0·41
RS 07-87	13	III	po-C	439	37·78	0·02	0·01	26·34	0·33	35·24	0·02	0·01	0·00	99·76	70·5	0·37
RS 07-88	10	III	po-C	461	35·92	0·02	0·02	35·75	0·66	27·93	0·02	0·01	0·01	100·42	58·2	0·78

n, number of analyses; Fo = 100[Mg/(Mg + Fe)]; Te = 100[Mn/(Mg + Fe + Mn).

display any significant variation, whereas P_2O_5 rises significantly in the pomica-C cumulates (to 10 wt %; average 2·45 wt %). Similar geochemical trends are observed in the three MCU of the Sept Iles layered series (Table 9) and in common mafic layered intrusions. However, in other intrusions, such as Skaergaard and Kiglapait, the evolved cumulate-rocks display a more important FeO_t enrichment. The absence of strong FeO_t enrichment in the Sept Iles gabbros probably results from the high Mg-number of the ferro-magnesian minerals, even in the evolved cumulates (pomica-C).

STRONTIUM ISOTOPES

Sr-isotope ratios and Sr and Rb concentrations have been determined in 20 plagioclase separates and one sample of gneissic country rock. The data are presented in Supplementary Dataset 8. When calculated at 564 Ma, the $^{87}Sr/^{86}Sr$ ratios of plagioclase range from 0·70360 to 0·70497. The sample of gneissic country rock has a much higher $(^{87}Sr/^{86}Sr)_{564}$ of 0·77457. Figure 7 displays the stratigraphic evolution of (Sr_i) in plagioclase separates from the layered series. It is worth noting that this evolution is strongly anti-correlated with the evolution of An%, Fo% and cpx Mg-number (not shown). Contamination of mantle-derived magmas by mixing with crustal material is expected to change the isotopic composition of magmas to higher values of $(^{87}Sr/^{86}Sr)_i$ (DePaolo & Wasserburg, 1979; DePaolo, 1981). DePaolo (1981) indicated that an increase of $(^{87}Sr/^{86}Sr)$ in the resident chamber magma depends on many parameters, including the volume of the resident magma, the volume of the contaminant magma and the degree of differentiation. In the Sept Iles layered series, $(^{87}Sr/^{86}Sr)_{564}$ increases upwards in each MCU, with the highest values observed at the top of MCU I and in the middle and upper part of MCU II (Fig. 7). Modelling taking into account the highest $(^{87}Sr/^{86}Sr)_{564}$ ratio of the layered series (0·70497) and the $(^{87}Sr/^{86}Sr)_{564}$ of the country rocks (0·77457) indicates that less than 2 vol. % assimilation of a country rock with this isotopic composition is required to explain the highest $(^{87}Sr/^{86}Sr)_{564}$value observed at the top of MCU II. However, a lower value of $(^{87}Sr/^{86}Sr)_{564}$ was estimated for the Sept Iles country rocks by taking into account

Table 4: Representative microprobe analyses of pyroxenes from the Sept Iles layered series

Sample no.	*n*	MCU	Cumulus assemblage	Height (m)	SiO_2	TiO_2	Al_2O_3	FeO_t	MnO	MgO	CaO	Na_2O	K_2O	Total	Mg-no.	Wo	Ens	Fs	Jo
Ca-rich pyroxene																			
9-2451	6	I	po-C	−4142	51·59	0·86	2·93	7·90	0·20	14·43	21·93	0·33	0·01	100·18	76·5	50·4	37·9	11·7	0·60
9-2111.5	4	I	po-C	−3864	51·22	0·83	2·52	8·94	0·26	14·15	20·89	0·34	0·01	99·16	73·8	48·8	37·8	13·4	0·77
9-1514.5	11	I	pomic-C	−3375	51·25	1·14	3·06	9·06	0·25	14·16	20·97	0·39	0·01	100·29	73·6	48·8	37·7	13·5	0·73
9-772.5	17	I	pmic-C	−2767	51·36	1·02	2·73	9·67	0·29	13·91	20·54	0·42	0·01	99·96	72·0	48·2	37·3	14·5	0·85
9-514	19	I	pomica-C	−2556	51·85	0·95	2·21	10·32	0·35	13·89	20·32	0·44	0·01	100·34	70·6	47·5	37·1	15·5	0·99
9-389	9	I	pomica-C	−2453	51·19	1·18	2·35	10·53	0·33	13·92	19·99	0·42	0·00	99·93	70·2	46·9	37·3	15·8	0·94
8-1917.5	13	II	pomi-C	−2255	50·55	1·26	3·42	8·82	0·24	14·61	20·45	0·45	0·01	99·81	74·7	47·8	39·0	13·2	0·69
8-1633.5	12	II	pomi-C	−2023	50·11	1·28	3·49	8·30	0·20	14·24	21·26	0·42	0·01	99·32	75·4	49·6	38·0	12·4	0·61
8-1264	11	II	pomi-C	−1700	50·65	1·09	3·04	8·50	0·23	14·23	21·31	0·40	0·01	99·47	74·9	49·5	37·8	12·7	0·69
8-814	19	II	pomic-C	−1352	50·67	1·25	3·13	8·51	0·26	14·21	21·06	0·42	0·01	99·51	74·9	49·3	38·0	12·8	0·77
8-118	21	II	pmic-C	−782	51·05	1·13	2·60	9·64	0·30	14·60	20·08	0·36	0·01	99·77	73·0	46·8	38·9	14·4	0·84
8-5.5	18	II	pmic-C	−690	51·49	0·90	2·29	9·28	0·32	14·23	21·20	0·37	0·00	100·08	73·2	48·8	37·5	13·7	0·91
LHS 05-40	18	II	pomic-C	−680	51·67	0·74	2·14	8·99	0·32	14·38	21·10	0·33	0·01	99·67	74·0	48·7	38·0	13·3	0·92
LHS 07-152	20	II	pmic-C	−222	51·24	0·74	2·59	8·49	0·27	14·37	21·69	0·31	0·01	99·71	75·1	49·8	37·7	12·5	0·80
LHS 07-158	23	II	pomica-C	0	51·82	0·56	1·78	10·20	0·35	14·08	20·82	0·31	0·01	99·93	71·1	47·9	37·0	15·1	1·00
LHS 07-159	15	II	pomica-C	52	51·55	0·52	1·43	12·19	0·42	13·19	20·27	0·34	0·01	99·97	65·9	47·0	34·9	18·1	1·19
RS 05-53	13	II	pomica-C	134	51·02	0·30	1·08	14·79	0·56	11·33	20·25	0·23	0·02	99·56	57·7	47·4	30·3	22·2	1·59
RS 07-120	16	II	pomica-C	150	51·37	0·31	1·09	15·64	0·60	10·82	20·18	0·24	0·00	100·24	55·2	47·4	29·1	23·6	1·71
RS 07-77	5	III	pomi-C	395	52·15	0·68	2·27	6·31	0·16	15·16	22·87	0·39	0·01	99·99	81·1	51·7	39·2	9·1	0·48
RS 07-87	4	III	po-C	439	51·86	0·69	2·46	5·77	0·17	15·23	22·74	0·42	0·02	99·35	82·5	51·9	39·7	8·4	0·53
RS 07-88	9	III	po-C	461	51·91	0·46	1·91	9·07	0·34	13·90	22·07	0·37	0·01	100·05	73·2	50·4	36·3	13·3	1·00
Orthopyroxene																			
9-2533.5	1	I	po-C	−4210	54·24	0·18	1·33	16·94	0·40	25·94	0·83	0·00	0·00	99·94	73·2				
9-2111.5	5	I	po-C	−3864	54·00	0·18	1·28	17·62	0·43	25·18	0·84	0·03	0·01	99·54	71·8				
8-5.5	3	II	pmic-C	−690	53·67	0·40	1·04	18·41	0·53	24·41	1·45	0·03	0·00	99·95	70·3				
LHS 07-159	15	II	pomica-C	52	51·68	0·26	0·67	25·54	0·77	19·29	1·42	0·03	0·01	99·68	57·4				
RS 05-53	6	II	pomica-C	134	50·34	0·18	0·50	30·64	1·05	15·03	1·40	0·02	0·02	99·19	46·7				
RS 07-120	10	II	pomica-C	150	50·17	0·15	0·50	31·95	1·11	13·88	1·66	0·01	–	99·42	43·6				
RS 07-73	11	III	pomi-C	351	53·87	0·03	1·40	18·39	0·35	25·69	0·19	0·02	0·01	99·94	71·4				
RS 07-77	7	III	pomi-C	395	54·10	0·05	1·15	18·03	0·36	25·54	0·24	0·02	0·01	99·50	71·6				
RS 07-88	9	III	po-C	461	53·05	0·26	0·89	18·08	0·63	25·61	1·26	0·03	0·01	99·82	71·6				

n, number of analyses; Mg-number = 100[Mg/(Mg + Fe)]; Wo = 100[Ca/(Mg + Fe + Ca)]; Ens = 100[Mg/(Mg + Fe + Ca)]; Fs = 100[Fe/(Mg + Fe + Ca)]; Jo = 100Mn/(Mg + Fe + Mn)].

the isotopic composition of sediments from the Moisie River ($^{87}Sr/^{86}Sr$ 0·7163; Wadleigh *et al.*, 1985), which drains the Sept Iles area, and the Rb and Sr contents of the Canadian Shield as a whole (110 and 316 ppm, respectively; Shaw *et al.*, 1986). This calculation gives a ($^{87}Sr/^{86}Sr$) ratio of 0·7084 for the host rocks at the time of the intrusion, suggesting that our estimation of the amount of upper crustal contamination could be a considerable underestimate. A lower crustal component could also have been involved in the contamination of the Sept Iles magmas. However, the lack of Nd and Pb isotopic data makes it impossible to evaluate this prospect.

PARENTAL MAGMA COMPOSITION

The compositions of fine-grained mafic rocks from the chilled margin (Sept Iles border zone) are reported in Table 10 and have been considered as the potential parental magma for the intrusion. Major element geochemical modelling using MELTS (Ghiorso & Sack, 1995) and

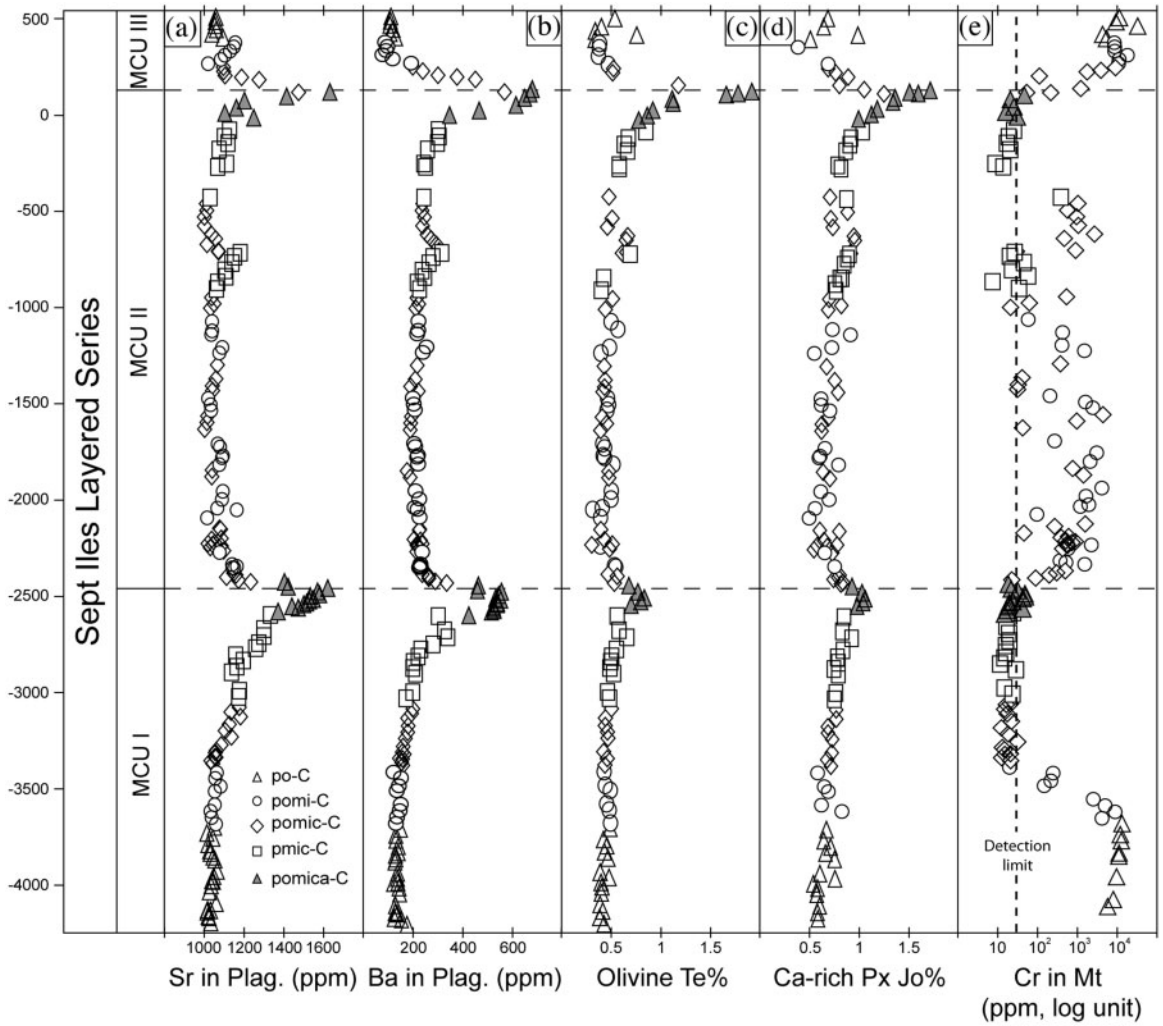

Fig. 8. Minor and trace element compositional variation of (a, b) plagioclase (Sr and Ba), (c) olivine (tephroite; Te%), (d) Ca-rich pyroxene (johannsenite; Jo%) and (e) magnetite (Cr) with stratigraphic position in the Sept Iles layered series. Dashed lines represent boundaries between MCU.

Table 5: Major (wt %) and trace (ppm) element compositions of separated magnetite from the Sept Iles layered series (XRF analyses)

Sample no.	MCU	Cumulus assemblage	Height (m)	SiO_2	TiO_2	Al_2O_3	Fe_2O_3	FeO	MnO	MgO	Total	X_{mt}	X_{usp}	Cr
9-2111.5	I	po-C	−3864	0·11	4·85	3·02	56·67	33·41	0·20	1·54	99·80	0·86	0·14	10516
9-1514.5	I	pomic-C	−3375	0·74	9·91	3·57	45·65	37·74	0·26	1·61	99·49	0·70	0·30	27·2
9-514	I	pomica-C	−2556	0·63	9·92	3·30	45·79	38·29	0·31	1·21	99·45	0·70	0·30	19·3
9-389	I	pomica-C	−2453	0·43	9·78	3·25	45·99	38·02	0·29	1·26	99·02	0·71	0·29	59·6
8-118	II	pmic-C	−782	0·39	7·04	3·26	51·55	35·48	0·22	1·37	99·32	0·79	0·21	28·4
8-5.5	II	pmic-C	−690	0·44	7·04	3·29	51·74	35·38	0·23	1·48	99·59	0·79	0·21	33·5
LHS 07-159	II	pomica-C	52	0·66	11·40	2·62	43·11	39·95	0·39	0·78	98·91	0·66	0·34	20·8
RS 05-53	II	pomica-C	134	0·61	16·48	1·54	34·38	44·72	0·45	0·57	98·76	0·51	0·49	57·7
RS 07-73	III	pomi-C	351	0·71	4·78	2·99	56·19	33·80	0·15	1·14	99·74	0·86	0·14	10550
RS 07-88	III	po-C	461	0·53	5·70	5·20	52·54	33·98	0·25	1·86	100·05	0·83	0·17	4251

FeO and Fe_2O_3 recalculated from Fe_2O_{3tot} by charge balance; molar fractions of magnetite and ulvöspinel (X_{mt} and X_{usp}) calculated following QUILF algorithm (Andersen *et al.*, 1993).

Table 6: Microprobe analyses of potassic-feldspar from the Sept Iles layered series

Sample no.	*n*	MCU	Cumulus assemblage	Height (m)	SiO_2	TiO_2	Al_2O_3	FeO_t	MgO	CaO	Na_2O	K_2O	Total	An	Ab	Or
LHS 07-159	2	II	pomica-C	52	65·31	0·07	19·18	0·17	0·00	0·77	3·67	10·25	99·42	3·9	33·9	62·2
RS 07-125	1	II	pomica-C	140	64·53	0·08	19·47	0·09	0·00	0·16	2·58	12·76	99·67	0·8	23·3	75·9
RS 07-120	1	II	pomica-C	150	63·23	0·02	19·01	0·07	0·00	0·11	1·09	14·59	98·12	0·6	10·1	89·3

n, number of analyses; An = 100[Ca/(Ca + Na + K)]; Ab = 100[Na/(Ca + Na + K)]; Or = 100[K/(Ca + Na + K)].

Table 7: Major (wt %) element compositions of separated ilmenite from the Sept Iles layered series (XRF analyses)

Sample no.	MCU	Cumulus assemblage	Height (m)	SiO_2	TiO_2	Al_2O_3	Fe_2O_3	FeO	MnO	MgO	Total	X_{geik}	X_{pyr}	X_{hem}	X_{ilm}
9-2111.5	I	po-C	−3864	0·03	49·50	0·13	8·03	37·59	0·48	3·61	99·36	0·133	0·010	0·075	0·781
9-1514.5	I	pomic-C	−3375	0·26	50·13	0·21	5·94	39·00	0·49	3·13	99·15	0·116	0·010	0·056	0·817
9-514	I	pomica-C	−2556	0·19	50·14	0·21	5·31	40·19	0·62	2·39	99·05	0·090	0·013	0·050	0·847
9-389	I	pomica-C	−2453	0·06	49·77	0·55	5·19	41·04	0·52	1·79	98·92	0·067	0·011	0·049	0·873
8-118	II	pmic-C	−782	0·14	50·84	0·26	4·73	39·46	0·57	3·18	99·18	0·118	0·012	0·044	0·826
8-5.5	II	pmic-C	−690	0·21	50·61	0·22	5·22	39·06	0·57	3·29	99·19	0·122	0·012	0·049	0·817
LHS 07-159	II	pomica-C	52	0·25	50·43	0·28	3·89	41·54	0·64	1·77	98·81	0·067	0·014	0·037	0·883
RS 05-53	II	pomica-C	134	0·17	49·61	0·27	4·05	42·58	0·89	0·63	98·21	0·024	0·019	0·039	0·917
RS 07-73	III	pomi-C	351	0·12	49·69	0·21	5·89	40·48	0·57	2·03	99·00	0·076	0·012	0·056	0·856
RS 07-88	III	po-C	461	0·25	48·63	0·36	8·89	37·08	0·68	3·35	99·25	0·124	0·014	0·083	0·778

FeO and Fe_2O_3 recalculated from Fe_2O_{3tot} by charge balance; molar fractions of geikielite, pyrophanite, hematite and ilmenite (X_{geik}, X_{pyr}, X_{hem}, X_{ilm}) calculated following QUILF algorithm (Andersen *et al.*, 1993).

published mineral–melt partition coefficients (e.g. Roeder & Emslie, 1970; Toplis, 2005) indicate that this magma is able to crystallize the most primitive mineral compositions (MCU I: An_{68}, Fo_{72}; MCU III: An_{72}, Fo_{71}) observed in the layered series (Table 10). The Sept Iles parental magma was thus a ferrobasalt that was relatively low in SiO_2 (*c.* 48 wt %), highly enriched in FeO_t (*c.* 15 wt %) and TiO_2 (*c.* 3 wt %), and moderately enriched in trace elements. In chondrite-normalized REE diagrams (Fig. 10a), the Sept Iles primitive liquids show slightly fractionated REE patterns with weak negative Eu anomalies (Eu/Eu*: 0·88–0·95). In N-MORB-normalized trace element diagrams (Fig. 10b), the Sept Iles liquids have trace element patterns that are moderately enriched compared with primary melts of the primitive mantle, with positive anomalies in Ba, Rb and K and negative anomalies in Nb, Ta, Sr, Zr and Hf. The enrichment in FeO_t and to a lesser extent in TiO_2 in the Sept Iles primitive magmas is highly significant compared with other classical ferrobasaltic layered intrusions (Table 10) such as the Skaergaard intrusion (Hoover, 1989*a*; Toplis & Carroll, 1995), the Ulvö Gabbro (Larson *et al.*, 2008) and the main and upper zones of the Bushveld complex (Tegner *et al.*, 2006). Enrichment in FeO_t and TiO_2 could result either from the mantle source composition or from previous fractionation of silicate phases. Typical primitive mantle-derived basaltic magmas have FeO_t contents between 7 and 10 wt % and TiO_2 contents between 0 and 1 wt % (Green *et al.*, 1979; McNeill & Danyushevsky, 1996; Falloon *et al.*, 1999; Danyushevsky *et al.*, 2003); however, fractional crystallization of silicate phases can also result in FeO_t and TiO_2 enrichment of residual liquids (e.g. Juster *et al.*, 1989; Snyder *et al.*, 1993; Toplis & Carroll, 1995; Thy *et al.*, 2006). The Sept Iles magma most probably represents an evolved basalt resulting from a previous process of fractionation of a more primitive magma. High FeO_t and TiO_2 basalts have also been observed in the Galapagos Spreading Centre and were interpreted by Juster *et al.* (1989) as

Table 8: Location and thickness of the main Fe–Ti oxide layers in the Sept Iles layered series

Sample no.	Stratigraphic position	Thickness (cm)
RS 07-116	270	34
RS 05-07*	111	9
RS 07-02*	89	26
LHS 07-157 (M4)	10	173
8-600.5	1186	9
8-620.3	1200	52
8-633.2	1211	450
8-660.0	1227	61
8-889.7	1415	173
8-981.5	1490	86
8-1068.0	1561	7
8-1112.5	1597	67
8-1309.0	1770	11
8-1469.0	1910	26
8-1492.0 (M3)	1930	1212
8-1539.3	1947	502
8-1571.3	1974	6
8-1611.8	2006	7
8-1648.7	2035	138
8-1661.0	2046	112
9-160.3 & 8-1877.5 & LHS 07-37 (M2)	2272	874
9-265.1 (M1)	2352	1584
9-1296.0	3198	5
9-1399.0	3281	182

*Nelsonite layers.
M1 to M4 Fe–Ti oxide layers are supposed to be responsible for the magnetic anomalies of the layered series.

resulting from 50% fractionation of a typical mid-ocean ridge basalt (MORB) composition. However, recent studies on continental flood basalts from the Central Atlantic Magmatic Province (Guyana and Guinea) have described high-Ti tholeiites (*c.* 49 wt % SiO_2; 3 wt % TiO_2; 15 wt % FeO_t) very close in composition to the Sept Iles liquids, suggesting that these liquids could result from only 10% of fractionation from a primitive mantle melt (Deckart *et al.*, 2005).

ORDER OF MINERAL APPEARANCE: GEOCHEMICAL CONSTRAINTS

The stratigraphic variation of mineral modes in the Sept Iles layered series suggests that Fe–Ti oxides join the liquidus before Ca-rich pyroxene (Fig. 6). This order of mineral appearance is opposite to that observed in most basaltic and ferrobasaltic experimental investigations and in the stratigraphy of common mafic layered intrusions (Thy & Lofgren, 1994; Galapagos Spreading Center: Juster *et al.*, 1989; McIntosh: Mathison & Hamlyn, 1987; Skaergaard: Hoover, 1989*b*; McBirney, 1989, 1996; Toplis & Carroll, 1995; Thy *et al.*, 2006; Potato River: Klewin, 1990; Newark Island: Snyder *et al.*, 1993; Wiebe & Snyder, 1993). As suggested by Means & Park (1994) and McBirney & Hunter (1995), petrographic and modal criteria cannot be used unambiguously to constrain petrogenetic interpretations. We thus present a complementary approach to constrain the timing of Ca-rich pyroxene and Fe–Ti oxide crystallization by using geochemical variations in mineral compositions.

Chromium is incompatible in the po-C plagioclase–olivine cumulates ($D_{Cr}^{Plag/Liq}=0$–$0{\cdot}02$; $D_{Cr}^{Ol/Liq}=0{\cdot}6$–$1{\cdot}8$; Bougault & Hekinian, 1974; Hart & Dunn, 1993; Beattie, 1994; Bindeman *et al.*, 1998; Aigner-Torres *et al.*, 2007) but is highly compatible in the Fe–Ti oxides-bearing cumulates (pomi-C, pomic-C, pmic-C and pomica-C; $D_{Cr}^{Mt/Liq}=50$–230; $D_{Cr}^{Ilm/Liq}=11$–43; Leeman *et al.*, 1978; Jensen *et al.*, 1993; Klemme *et al.*, 2006; Charlier *et al.*, 2007). Figure 11a is a close-up showing the evolution of the Cr content of magnetite within MCU I. From the base to the top, Cr first increases from 5600 to 12 300 ppm, before decreasing at −3680 m to concentrations below the detection limit. The upward increase of the Cr content of magnetite reflects an increase in the Cr content of the residual liquid as a result of silicate fractionation, suggesting that Fe–Ti oxides are interstitial phases. The decrease in the magnetite Cr content starts at the stratigraphic level at which Fe–Ti oxides become abundant, suggesting that these minerals join the liquidus in the main magma body at this level. The geochemical evolution of Cr in magnetite thus confirms the previously established po-C to pomi-C type subdivision of cumulates from the lower part of MCU I.

In the lower part of MCU I, Ca-rich pyroxene is a subordinate phase with a poikilitic habit. The intercumulus status of poikilitic Ca-rich pyroxene has long been accepted by igneous petrologists (e.g. McBirney, 1996; Wager & Brown, 1998). However, this interpretation is now being re-examined in the Skaergaard intrusion. Indeed, recent studies by Holness *et al.* (2007*a*, 2007*b*) suggested that poikilitic Ca-rich pyroxene could be a cumulus phase, at least in the upper part of the Skaergaard LZa. In the Sept Iles layered series, the Sr content of plagioclase from cumulates containing poikilitic Ca-rich pyroxene (po-C and pomi-C) does not display any significant variation (Fig. 11b). This is easily explained by a D_{Sr}^{Bulk} close to unity, resulting from the high mode of plagioclase (*c.* 70 wt %), a value of $D_{Sr}^{Plag/Liq}$ close to 1·5 (Bindeman

Table 9: Average major (%) element composition and average mineral modes of the different cumulus assemblages in the Sept Iles layered series (XRF analyses)

MCU:	I	I	I	I	I	II	II	II	II	III	III	III
Cumulate type:	po	pomi	pomic	pmic	pomica	pomi	pomic	pmic	pomica	po	pomi	pomic
n:	21	8	13	10	13	26	50	20	5	7	6	5
SiO_2	47·05	40·43	40·90	41·33	40·62	38·45	41·44	39·4	38·03	45·38	46·32	41·17
TiO_2	0·55	3·36	4·89	6·00	4·09	4·99	4·47	7·11	5·4	1·18	1·1	5·68
Al_2O_3	21·82	18·81	15·94	15·17	15·79	17·06	16·52	13·39	11·83	20·65	20·43	16·13
FeO_t	8·28	17·38	17·54	16·93	15·65	20·18	16·73	20·02	21·29	10·11	10·88	18·55
MnO	0·11	0·15	0·16	0·18	0·22	0·17	0·17	0·2	0·36	0·12	0·12	0·18
MgO	8·80	7·61	7·31	6·21	6·49	7·40	7·36	6·62	6·52	8·69	9·11	6·66
CaO	10·15	8·70	10·47	11·01	11·02	8·77	10·38	10·94	10·54	10·11	8·74	7·57
Na_2O	2·77	2·58	2·69	3·00	3·19	2·46	2·5	2·15	2·56	2·31	2·73	3·4
K_2O	0·22	0·19	0·18	0·19	0·21	0·17	0·16	0·13	0·31	0·29	0·33	0·32
P_2O_5	0·05	0·04	0·02	0·03	2·32	0·03	0·04	0·05	2·57	0·11	0·09	0·11
Total	99·80	99·25	100·10	100·05	99·60	99·68	99·77	100·01	99·41	99·07	99·99	99·93
Mg-no.	65·45	43·84	42·63	39·54	42·5	39·54	43·95	37·08	35·31	60·51	59·88	39·02
Plagioclase	68·2	52·2	43·8	44·6	50·4	54·5	45·6	38·6	39·5	64·2	63·6	49·7
Olivine	27·8	24·6	9·3	6·0	16·3	19·5	10·7	2·3	16·5	30·9	28·2	2·5
Ca-rich pyroxene	2·1	1·3	24·4	27·4	12·1	2·0	20·3	29·9	15·9	2·4	1·3	26·0
Magnetite	0·7	13·9	11·9	11·7	8·8	17·3	13·3	16·4	15·1	1·1	5·0	14·7
Ilmenite	1·2	7·9	10·7	10·3	7·0	6·7	10·1	12·7	8·6	1·5	2·0	7·1
Apatite	0·0	0·0	0·0	0·0	5·4	0·0	0·0	0·0	5·5	0·0	0·0	0·0

n, number of samples. Mg-number = 100[Mg/(Mg + Fe)]. Cumulus assemblages following the nomenclature of Irvine (1982). Mineral abbreviations in cumulus assemblages: p, plagioclase; o, olivine; m, magnetite; i, ilmenite; c, Ca-rich pyroxene; a, apatite.

et al., 1998) and the incompatible behaviour of Sr in olivine and Fe–Ti oxides (Beattie, 1994; Ewart & Griffin, 1994). When Ca-rich pyroxene becomes tabular in habit (pomic-C), its mineral mode increases abruptly to 40 wt %. As a result of the low $D_{Sr}^{Cpx/Liq}$ (*c.* 0·1; Hart & Dunn, 1993; Vannucci *et al.*, 1998), the crystallization of abundant Ca-rich pyroxenes substantially lowers the D_{Sr}^{Bulk} to a value close to 0·75, causing Sr to become incompatible. The Sr content of the residual liquid and plagioclase thus starts to increase with further differentiation. This change of Sr behaviour in plagioclase when Ca-rich pyroxene becomes tabular suggests that the appearance of this habit represents the timing of cumulus Ca-rich pyroxene crystallization, in perfect agreement with the pomi-C to pomic-C cumulate transition defined on the basis of mineral modes and textures.

Combined geochemical evolution of Cr in magnetite and Sr in plagioclase thus supports the petrographic hypothesis of early saturation of Fe–Ti oxides in the Sept Iles cumulates, before the appearance of cumulus Ca-rich pyroxene. The sequence of crystallization in the Sept Iles layered series is thus plagioclase and olivine, followed by Fe–Ti oxides, then Ca-rich pyroxene and finally apatite. In addition to petrographic constraints, the saturation of apatite is also geochemically illustrated by a marked jump in the whole-rock P_2O_5 content in pomica-C cumulates (Fig. 9).

Early saturation of Fe–Ti oxides

The timing of Fe–Ti oxide saturation in the Sept Iles layered series can be compared with other well-studied ferrobasaltic and ferropicritic layered intrusions on the basis of the silicate phase compositional data (Table 11). The saturation of Fe–Ti oxides in mafic layered intrusions commonly occurs at an advanced stage of differentiation (ranging from $F = 64\%$ in the upper and main zones of the Bushveld complex to $F = 10\%$ in Kiglapait, where F is the fraction of remaining liquid). Except in the Panzhihua intrusion (China) and to a lesser extent in the Bushveld complex, the compositions of the silicate phases in equilibrium with the first liquidus Fe–Ti oxides are highly evolved in most layered intrusions (e.g. $An_{45–53}$, $Fo_{55–56}$, cpx Mg-number 64–75). In contrast to these intrusions, the silicate minerals in the Sept Iles layered series are relatively

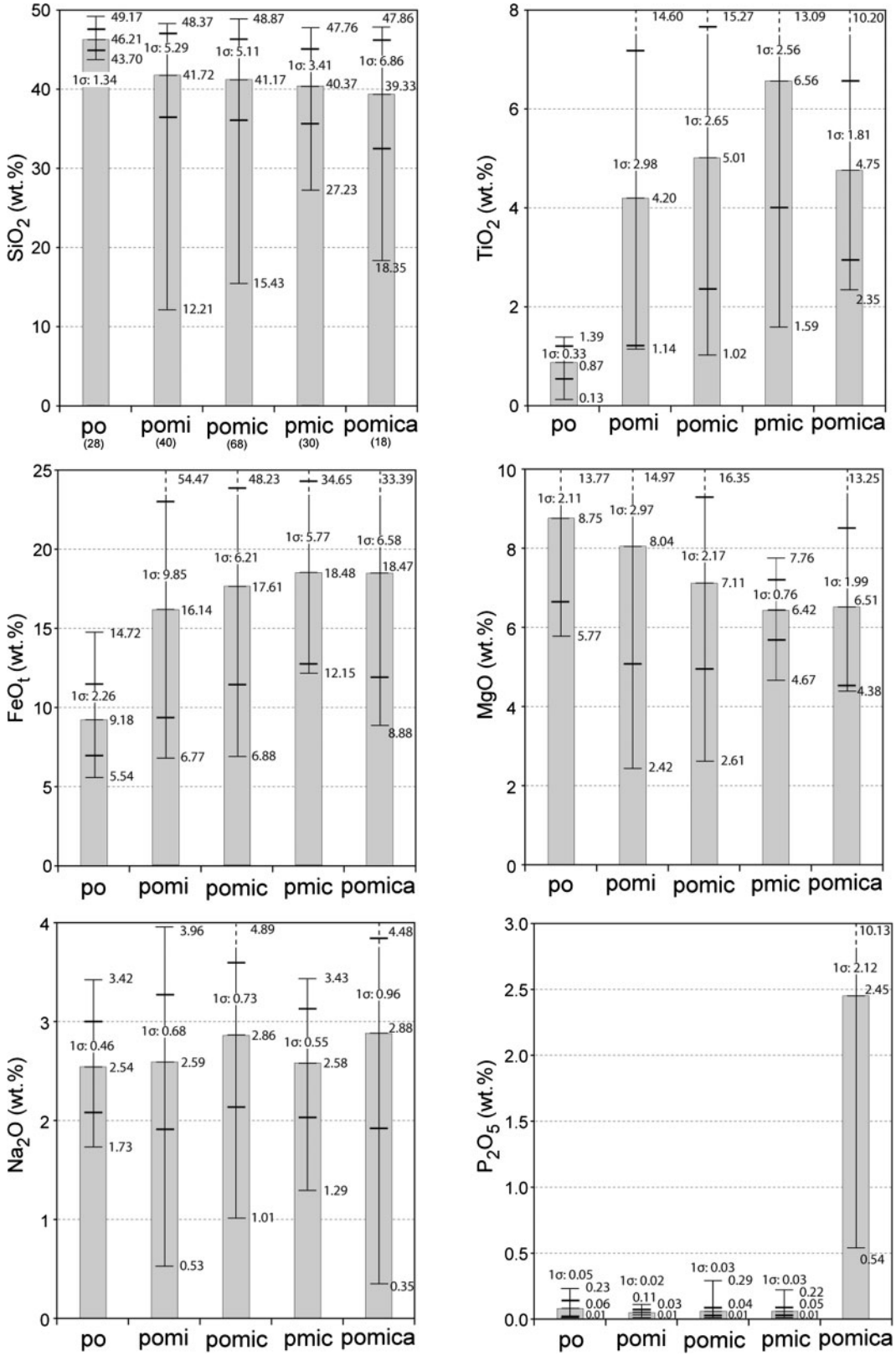

Fig. 9. Histograms of average major element compositions of whole-rock cumulates classified following their cumulus assemblages. The range of composition (grey bars) and 1σ standard deviation (fine lines) are shown for each cumulus assemblage. The number of samples in each assemblage is indicated below the assemblage name in the first histogram on the left.

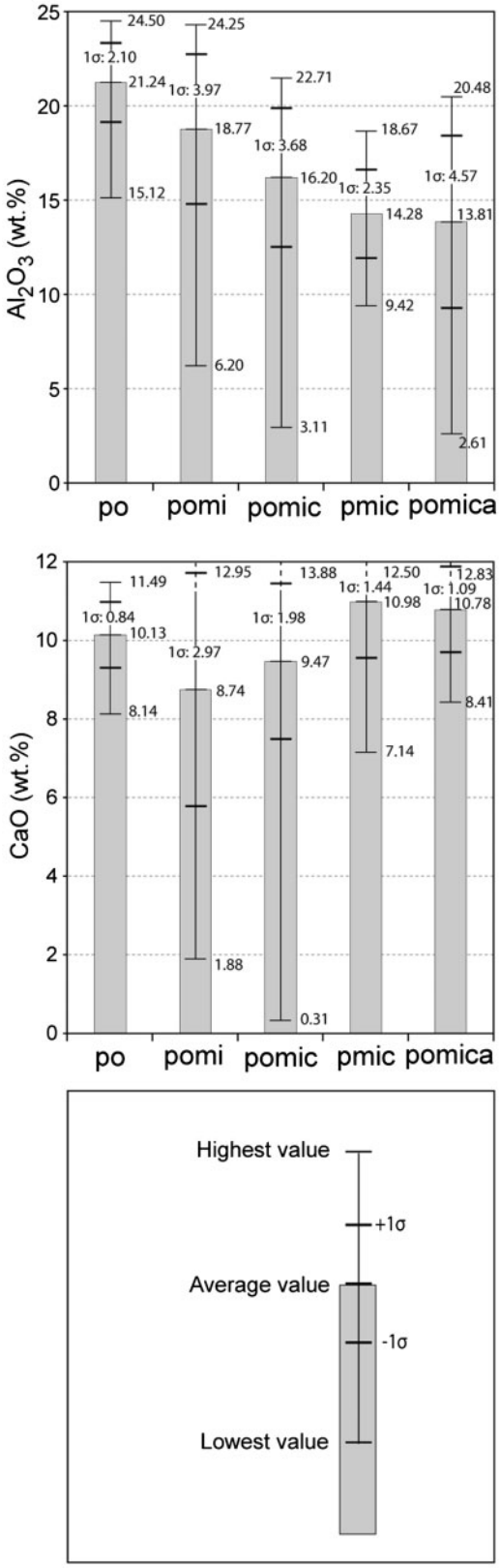

Fig. 9. Continued.

primitive at the onset of Fe–Ti oxide saturation (An_{61}, Fo_{66}). Apatite also crystallizes early in the Sept Iles layered series compared to other ferrobasaltic intrusions (Table 11). This behaviour is in agreement with the experimental data of Toplis *et al.* (1994), indicating that crystallization of magnetite lowers the solubility of phosphorus in basaltic melts.

The early saturation of Fe–Ti oxides in the Sept Iles magmas can result from three parameters: (1) the composition of the parental magma; (2) the fO_2 conditions; (3) the presence of volatiles in the magma. Toplis & Carroll (1995) have performed 1 atm dry experiments on a Skaergaard-like composition (SCl: 13·1 wt % FeO_t, 2·9 wt % TiO_2, 10·9 wt % CaO, 11·6 wt % normative wollastonite; Fig. 12a), and Snyder *et al.* (1993) have made 1 atm dry experiments on an evolved ferrobasalt related to the Newark Island intrusion (4–83C: 17·6 wt % FeO_t, 3·8 wt % TiO_2, 7·6 wt % CaO, 8·0 wt % normative wollastonite; Fig. 12b). Plagioclase and olivine are the first liquidus phases in the two sets of experiments. In the experiments of Toplis & Carroll (1995), Ca-rich pyroxene is the third crystallizing phase, with a liquidus temperature decreasing from 1140°C at FMQ+1 (where FMQ is the fayalite–magnetite–quartz buffer) to 1111 °C at FMQ − 2. Iron–titanium oxides are the last phases to appear. In contrast, in the experiments of Snyder *et al.* (1993), the crystallization of Ca-rich pyroxene is delayed to lower temperatures (1082–1090°C; FMQ − 3 to FMQ+0·5) and Fe–Ti oxides are liquidus phases before Ca-rich pyroxene. The experiments by Toplis & Carroll (1995) and Snyder *et al.* (1993) were carried out under similar conditions of pressure and fO_2. The different sequences of crystallization are thus related to the composition of the starting material. The CaO/FeO_t and CaO/TiO_2ratios and the normative wollastonite content are higher in the starting composition of Toplis & Carroll (1995) than in the starting composition of Snyder *et al.* (1993) and are thus probably the most fundamental parameters controlling the relative crystallization of Ca-rich pyroxene and Fe–Ti oxides. The Sept Iles parental magma has a composition that is intermediate between SCl and 4-83 C in terms of FeO_t and TiO_2 contents, CaO/FeO_t and CaO/TiO_2 ratios, and normative wollastonite. Its relatively low CaO content together with high FeO_t and TiO_2 contents compared with SCl could thus be the key parameter controlling the relative order of crystallization between Fe–Ti oxides and Ca-rich pyroxene.

Oxygen fugacity has a great influence on the stability of Fe–Ti oxides (Toplis & Carroll, 1995). Under highly oxidized conditions (>FMQ+2), SCl crystallizes magnetite early and probably before Ca-rich pyroxene (Fig. 12a). In experiments on SCl, FMQ conditions are required for simultaneous crystallization of magnetite and ilmenite. However, this saturation of Fe–Ti oxides occurs well after that of Ca-rich pyroxene. In the Sept Iles layered series,

Table 10: Major (%) and trace (ppm) element composition of fine-grained rocks from the Sept Iles layered intrusion and comparison with magma compositions of ferrobasaltic layered intrusions

Sample:	07-180	07-01	07-48	05-45	Average		4-83C	SC1
Rock-type:	MG	Dyke	MG	MG				
Location:	SI BZ	SI LS	SI BZ	SI BZ		UG	NI	Sk
SiO_2	48·53	48·51	48·65	48·56	48·56	46·82	46·12	48·30
TiO_2	2·82	2·88	2·78	2·91	2·85	2·40	3·82	2·90
Al_2O_3	14·67	14·13	14·59	14·62	14·50	16·11	13·38	14·90
FeO_t	14·50	14·82	15·06	15·10	14·87	13·72	17·64	13·10
MnO	0·21	0·23	0·21	0·29	0·24	0·20	0·22	–
MgO	5·65	5·56	5·14	5·53	5·47	6·32	4·65	6·50
CaO	9·79	9·61	9·47	9·97	9·71	8·77	7·57	10·90
Na_2O	2·63	2·76	2·81	2·90	2·78	3·08	3·55	2·70
K_2O	0·77	0·60	0·90	0·83	0·78	1·07	1·03	0·30
P_2O_5	0·82	0·72	0·36	0·36	0·57	0·40	0·35	–
LOI	0·03	0·23	0·23	0·00	–		1·16	–
Total	100·42	100·05	100·20	101·07	100·33	98·89	99·49	99·60
CaO/FeO_t	0·68	0·65	0·63	0·66	0·65	0·64	0·43	0·83
CaO/TiO_2	3·47	3·34	3·41	3·43	3·41	3·65	1·98	3·76
Rb	8·03	16·2	18·1	8·97	12·8	–	–	–
Ba	515	509	421	458	476	–	–	–
Sr	523	531	517	472	511	–	–	–
Y	49·1	50·0	54·2	45·7	49·7	–	–	–
Cr	56·5	54·0	41·3	41·6	48·4	–	–	–
V	214	258	257	233	241	–	–	–
Zr	126	126	264	90·8	152	–	–	–
Th	–	0·957	–	0·741	0·849	–	–	–
Hf	–	3·52	–	2·81	3·17	–	–	–
Nb	–	13·5	–	12·2	12·9	–	–	–
Ta	–	0·936	–	0·995	0·966	–	–	–
La	–	42·2	–	32·4	37·3	–	–	–
Ce	–	86·3	–	72·1	79·2	–	–	–
Pr	–	11·8	–	10·5	11·2	–	–	–
Nd	–	52·2	–	42·4	47·3	–	–	–
Sm	–	10·5	–	9·31	9·91	–	–	–
Eu	–	3·10	–	2·92	3·01	–	–	–
Gd	–	11·4	–	9·61	10·5	–	–	–
Tb	–	–	–	1·42	1·42	–	–	–
Dy	–	10·7	–	8·49	9·60	–	–	–
Ho	–	2·12	–	1·82	1·97	–	–	–
Er	–	6·00	–	4·96	5·48	–	–	–
Tm	–	–	–	0·699	0·699	–	–	–
Yb	–	5·59	–	5·58	5·59	–	–	–
Lu	–	0·876	–	0·581	0·729	–	–	–
Eu/Eu*	–	0·88	–	0·95	0·91	–	–	–
Liquidus T (°C)[1]	1165	1167	1168	1171	1167	1191	1150	1158
Ln fO_2 at FMQ[2]	−20·40	−20·34	−20·23	−20·17	−20·34	−19·61	–	−20·54
Olivine (Fo) at FMQ[3]	74	73	72	73	72	–	–	–
Plag (An) at FMQ[3]	69	67	69	70	69	–	–	–

(Continued)

Table 10: Continued

Sample:	07-180	07-01	07-48	05-45	Average		4-83C	SC1
Rock-type:	MG	Dyke	MG	MG				
Location:	SI BZ	SI LS	SI BZ	SI BZ		UG	NI	Sk
K_d(Mg–Fe) oliv–melt[4]	0·300	0·300	0·299	0·300	0·300	–	–	–
Molecular norms								
Or	4·53	3·55	5·31	4·85	4·85	6·39	6·21	4·60
Pl								
(Ab)	22·10	23·32	23·70	24·20	24·20	26·27	29·50	22·79
(An)	25·76	24·35	24·46	24·08	24·08	27·18	18·48	26·18
Di								
(Wo)	7·21	7·80	8·41	9·38	9·38	5·90	7·96	11·63
(Ens)	3·22	3·42	3·50	4·06	4·06	2·85	2·83	6·10
(Fs)	3·95	4·36	4·95	5·32	5·32	2·96	5·22	5·20
Hy								
(Ens)	9·15	9·19	6·10	3·91	3·91	0·37	–	2·58
(Fs)	11·21	11·72	8·61	5·13	5·13	0·38	–	2·19
Ol								
(Fo)	1·17	0·90	2·26	3·98	3·98	8·91	6·33	5·30
(Fa)	1·58	1·27	3·53	5·76	5·76	10·24	13·17	4·98
Ilm	5·33	5·47	5·27	5·46	5·46	4·60	7·43	5·51
Mt	2·92	3·00	3·07	3·05	3·05	3·03	2·35	2·94
Ap	1·88	1·66	0·83	0·82	0·82	0·93	0·52	–

SI, Sept Iles; MG, marginal gabbro; BZ, border zone, LS, layered series; UG, Ulvö Gabbro; NI, Newark Island; Sk, Skaergaard.
[1]Liquidus temperature at FMQ determined using MELTS (Ghiorso & Sack, 1995) for Sept Iles samples and data from Toplis & Carroll (1995) and Snyder *et al.* (1993) for SC1 and 4-83C.
[2]Ln fO_2 calculated following O'Neill (1987) at the liquidus temperature and FMQ conditions.
[3]Plagioclase and olivine compositions predicted by MELTS at the liquidus temperature and FMQ conditions.
[4]Estimation of the K_d(Mg–Fe) between liquids and the most primitive olivine of MCU I (Fo 72·2). Calculations following the equations of Toplis (2005) with FeO/Fe_2O_3 ratios of liquids calculated following Kress & Carmichael (1991).

the petrography indicates that magnetite and ilmenite appear simultaneously as cumulus phases. The experiments of Toplis & Carroll (1995) thus indicate that a relatively low FeO_t and TiO_2 parent magma such as SCl cannot produce the Sept Iles sequence of crystallization, even under highly oxidized conditions. Recent 1 atm experiments have been performed by Botcharnikov *et al.* (2008) on a hydrous ferrobasalt similar to the SCl composition of Toplis & Carroll (1995). Water lowers the liquidus temperature of silicate phases, mainly plagioclase, which saturates after Ca-rich pyroxene at low water contents and after Ca-rich pyroxene and Fe–Ti oxides at high water contents (Fig. 12c). Addition of water to a parent magma similar to SCl thus means that the sequence of crystallization observed at Sept Iles cannot be reproduced.

Examination of experimental phase equilibria thus indicates that neither highly oxidized conditions nor high H_2O contents in the magma can result in the early saturation of Fe–Ti oxides from a relatively low FeO_t and TiO_2 parental magma such as SCl. Combined high FeO_t/CaO and TiO_2/CaO and the low wollastonite content of the Sept Iles magma are thus the most convincing explanation for the early saturation of Fe–Ti oxides.

FILLING OF THE MAGMA CHAMBER

Compositional reversals across MCU

After normal differentiation trends in MCU I and MCU II, large up-section increases in An%, Fo%, cpx Mg-number and Cr_{Mt} and decreases in $(^{87}Sr/^{86}Sr)_{564}$ are observed at the base of MCU II and MCU III (Fig. 7). Cumulus apatite and Ca-rich pyroxene disappear temporarily at these stratigraphic levels. Cumulus Fe–Ti oxides also disappear at the base of MCU III. Mineral compositions at the top of MCU I (An_{51}, Fo_{55}, cpx Mg-number 69) and MCU II (An_{34}, Fo_{21}, cpx Mg-number 55) are relatively primitive compared with the most evolved minerals

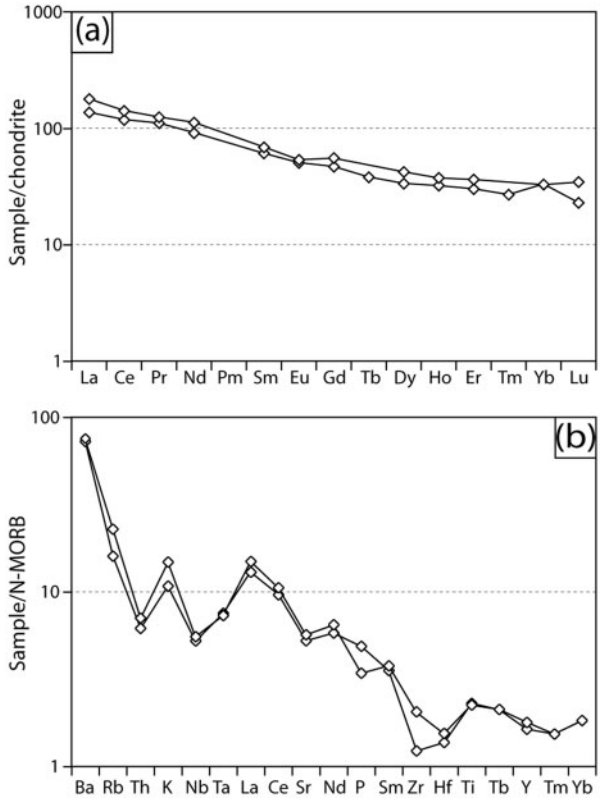

Fig. 10. (a) Chondrite-normalized REE patterns of fine-grained mafic samples from the chilled margin (Sept Iles border zone). (b) N-MORB-normalized trace element patterns of fine-grained mafic samples from the chilled margin. Chondrite and N-MORB normalizing values from Sun & McDonough (1989).

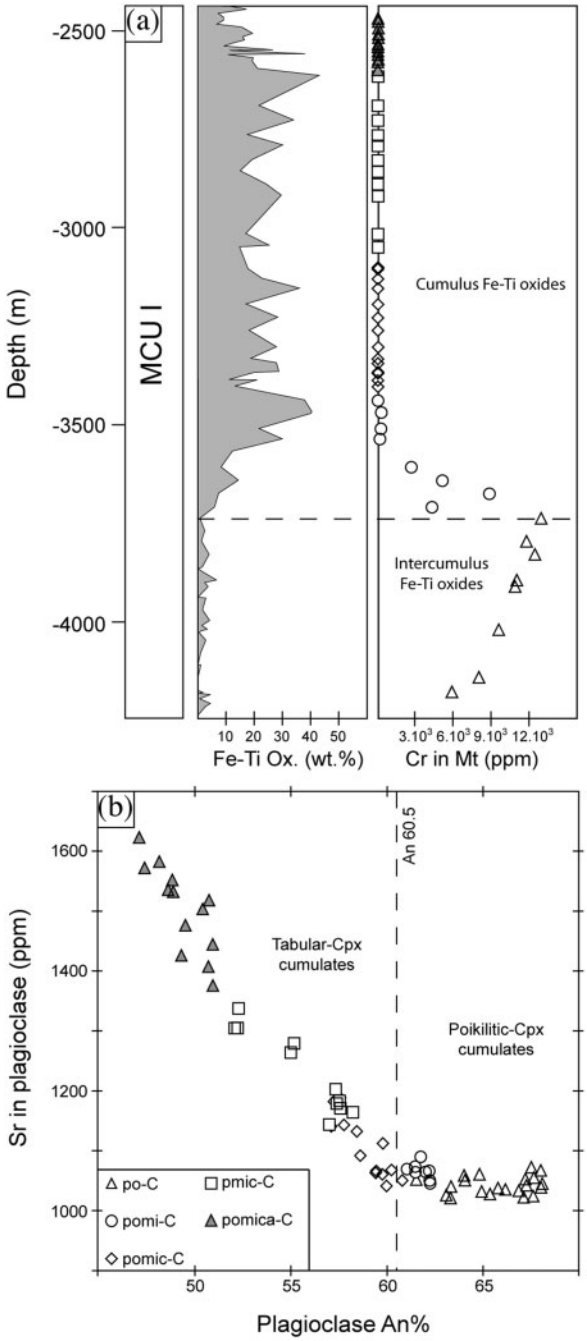

Fig. 11. (a) Stratigraphic variation of Fe–Ti oxide mode and Cr content in magnetite in MCU I. Dashed line represents the onset of cumulus Fe–Ti oxide crystallization (see text for explanation). (b) Variation of An (%) vs Sr (ppm) in plagioclase separates from MCU I. (Note the change in the slope at $An_{60\cdot5}$, when Ca-rich pyroxene becomes tabular.) Ox, oxides; Mt, magnetite; Cpx, Ca-rich pyroxene.

of common ferrobasaltic layered intrusions such as Skaergaard (An_{25}, Fo_0, cpx Mg-number 0) and Newark Island (An_{37}, Fo_{11}, cpx Mg-number 40). The liquids that crystallized MCU I and MCU II thus did not evolve to extreme differentiates. Large magma chamber replenishments are invoked to explain the cessation of magmatic differentiation in MCU I and MCU II as well as the observed shifts in mineral compositions and Sr isotope ratios at the base of MCU II and MCU III. The retrograde change in mineral compositions in reversals indicates that extensive mixing must have occurred during replenishment. Similar progressive magma chamber replenishments have been observed in the Fongen–Hyllingen layered intrusion (Wilson & Sorensen, 1996).

The basal reversal within MCU III reaches mineral compositions with An%, Fo% and cpx Mg-number similar to those observed at the base of MCU I. In contrast, minerals from the basal reversal of MCU II do not reach such primitive compositions. This dissimilarity indicates that the hybrid magma that crystallized MCU III was more primitive than that forming MCU II. The most evolved minerals from the Sept Iles layered series are observed at the top of MCU II, suggesting that MCU II has probably experienced a longer differentiation interval than MCU I before magma replenishment. It can thus be inferred that the proportion of residual liquid left at the

Table 11: Composition of silicate minerals and proportion of residual liquid at the saturation of Fe-Ti oxide, Ca-rich pyroxene and apatite in common layered intrusions

Phases	Sept Iles MCU I	Sept Iles MCU II	Skaergaard[1]	Newark Isl[2]	Bushveld[3] MUZ	Kiglapait[4]	Panzizhua[5]	Bjerkreim[6] Sokndal
Ca-rich pyroxene saturation								
Plagioclase (An)	60	60	66	53	72	53	73	46
Olivine (Fo)	66	68	68	60	-	65	82	-
F	-	-	80	57	100	15	100	-
Fe-Ti oxides saturation								
Plagioclase (An)	61	-	53	47	61	45	69	50
Olivine (Fo)	66	-	56	55	-	56	71	-
Ca-rich pyroxene (Mg#)	-	-	65	64	67	70	79	75
F	-	-	55	38	64	10	-	-
Apatite saturation								
Plagioclase (An)	60	57	39	40	49	41	53	46
Olivine (Fo)	51	52	31	26	34	39	65	-
Ca-rich pyroxene (Mg#)	71	71	44	43	57	56	76	72
F	-	-	<23	-	54	5	-	47

F = fraction of residual liquid; Bushveld MUZ = main and upper zones of the Bushveld above the pyroxenite marker, following Tegner et al. (2006). [1]McBirney, 1989; McBirney, 1996; Toplis & Carroll, 1995; [2]Wiebe, 1988; Wiebe & Snyder, 1993; Snyder *et al.*, 1993; [3]Tegner et al., 2006; [4]Morse, 1979; [5]Pang et al., 2009. [6]Wilson et al., 1996; Duchesne & Charlier, 2005.

top of MCU II was low. Volcanic eruptions could also have contributed to lower the proportion of residual magma at the top of MCU II. Consequently, when replenishment occurred at the base of MCU III, the low proportion of resident magma residual from MCU II was mixed with the primitive replenishing magma and the hybrid magma crystallized minerals with high An%, Fo% and cpx Mg-number. In contrast, the replenishing magma at the base of MCU II was mixed with a higher proportion of resident magma residual from MCU I and thus crystallized less primitive minerals at the base of MCU II. The rapid and strong increase in $(^{87}Sr/^{86}Sr)_{564}$ at the end of the MCU II also indicates that the amount of residual magma was lower, the amount of crustal contamination increasing with the disappearance of the magma. Obviously, the relative proportions of injected and replenishing magma must have influenced the composition of the hybrid magmas that crystallized MCU II and MCU III.

Compositional reversals inside MCU

Small progressive reversals to more primitive mineral compositions (*c.* 1–4% An, *c.* 3% Fo and cpx Mg-number, *c.* 500-4000 ppm Cr in magnetite) and intermittent disappearance of Ca-rich pyroxene are observed within the lower part of MCU II (from −2500 to −700 m), leading to the subdivision of MCU II into seven cyclic units (Fig. 13), where pomi-C and pomic-C cumulates alternate. The vertical intervals through which reversals occur are frequently in the range between 20 and 100 m.

Sample-to-sample An, Fo and cpx Mg-number variation of 1–2% can be considered as lying within the inherent variation of the process of crystallization (Cawthorn & Ashwal, 2009). However, variations exceeding this value are considered as indicating perturbation in the crystallization process. Reversals cannot be explained by closed-system crystal fractionation. Pressure and fO_2 variations, mixing between magma sheets in a stratified magma chamber or magma chamber replenishments are classically suggested to explain such compositional reversals and mineral disappearances.

During magma chamber replenishment, the injected magma can mix with the resident magma when there is a low-density contrast (Campbell & Turner, 1986, 1989) or if there is a high injection rate (Wiebe & Snyder, 1993). Mixing between primitive and resident magma is able to produce hybrid melts with increasingly higher Mg/Fe, Ca/Na and Cr contents as injection occurs. Magma mixing can also force the hybrid melt to leave the cotectic curve where a cumulus phase was crystallizing. Magma chamber replenishments and magma mixing between primitive and resident magmas are thus able to explain the reversals

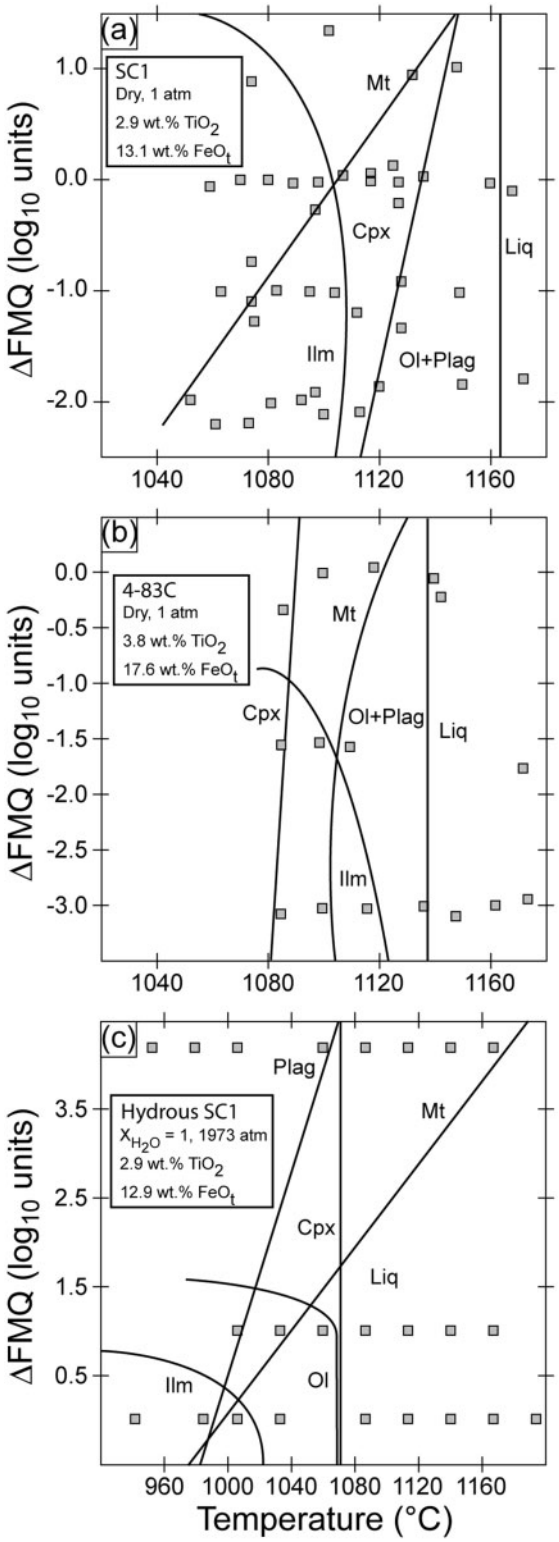

Fig. 12. Experimentally determined phase equilibria in ferrobasaltic melts as a function of oxygen fugacity and temperature. (a) Phase equilibria from 1 atm experiments on dry ferrobasalt (SC1) with 13 wt % FeO_t and 3 wt % TiO_2 from Toplis & Carroll (1995). (b) Phase equilibria from 1 atm experiments on dry ferrobasalt (4-83C) with 18 wt % FeO_t and 4 wt % TiO_2 from Snyder *et al.* (1993). (c) Phase equilibria from 1970 atm experiments on hydrous ferrobasalt (hydrous SC1) from Botcharnikov *et al.* (2008).

in mineral compositions (plagioclase, olivine, Ca-rich pyroxene and magnetite) as well as the temporary disappearance of Ca-rich pyroxene observed at the top of the cyclic units from MCU II.

A substantial decrease of the pressure during crystallization can change the location of the cotectic boundaries in basaltic systems, leading to the temporary disappearance of cumulus phases (Cameron, 1978, 1980; Osborn, 1980). Pressure decrease also causes the An content of plagioclase and the Mg-number of ferromagnesian minerals to increase (Osborn, 1980; Panjasawatwong *et al.*, 1995). However, Hatton (1984) indicated that a pressure decrease of at least 17 kbar is required to increase the Mg-number of ferromagnesian minerals by 3%. Such a large pressure variation is unrealistic in a subsurface layered intrusion such as Sept Iles.

Oxygen fugacity largely influences the composition of ferromagnesian minerals, as a result of its control on the redox state of the magma. Oxygen fugacity has, however, no influence on the Ca/Na partitioning between plagioclase and melt (Toplis & Carroll, 1995; Berndt *et al.*, 2005; Feig *et al.*, 2006). Progressive increase of fO_2 during crystallization could thus explain the reversals observed in ferromagnesian minerals within MCU II but cannot explain the reversals observed in plagioclase composition. In addition, increasing fO_2 lowers the mineral/melt partition coefficient of multi-valence elements (Toplis & Corgne, 2002). Chromium reversals at cycle boundaries cannot thus be achieved by fO_2 increase.

Intense convection in a stratified magma chamber can mix magmas from different compositional layers. Reversals in mineral composition can result from this magma mixing. Tegner *et al.* (2006) identified nine cyclic units in the upper and main zones of the Bushveld complex. The upper boundary of each cycle displays reversals in mineral composition and cumulus apatite disappearance. Tegner *et al.* (2006) interpreted these cycles as resulting from magma mixing between two magma layers in a stratified magma chamber. Before cumulus magnetite saturation, fractional crystallization increases the density of the residual melt and a stratified magma chamber can develop. When magnetite starts to crystallize, the melt density of the basal layer decreases. When the density becomes equal to that of the overlying layer, magmas from the two layers can mix by breakdown of the diffusive boundary (Tegner *et al.*, 2006). Cyclic units in the Sept Iles MCU II are remarkably similar to those of the Bushveld upper and main zones. However, in the Sept Iles layered series, Fe–Ti oxides are cumulus phases before the first reversal within MCU II. Reversals thus do not correlate with the appearance of a new cumulus phase, suggesting that no significant change in melt density is expected at the onset of the reversals. Mixing between zoned magma sheets is thus unlikely to explain the cyclic units of Sept Iles MCU II.

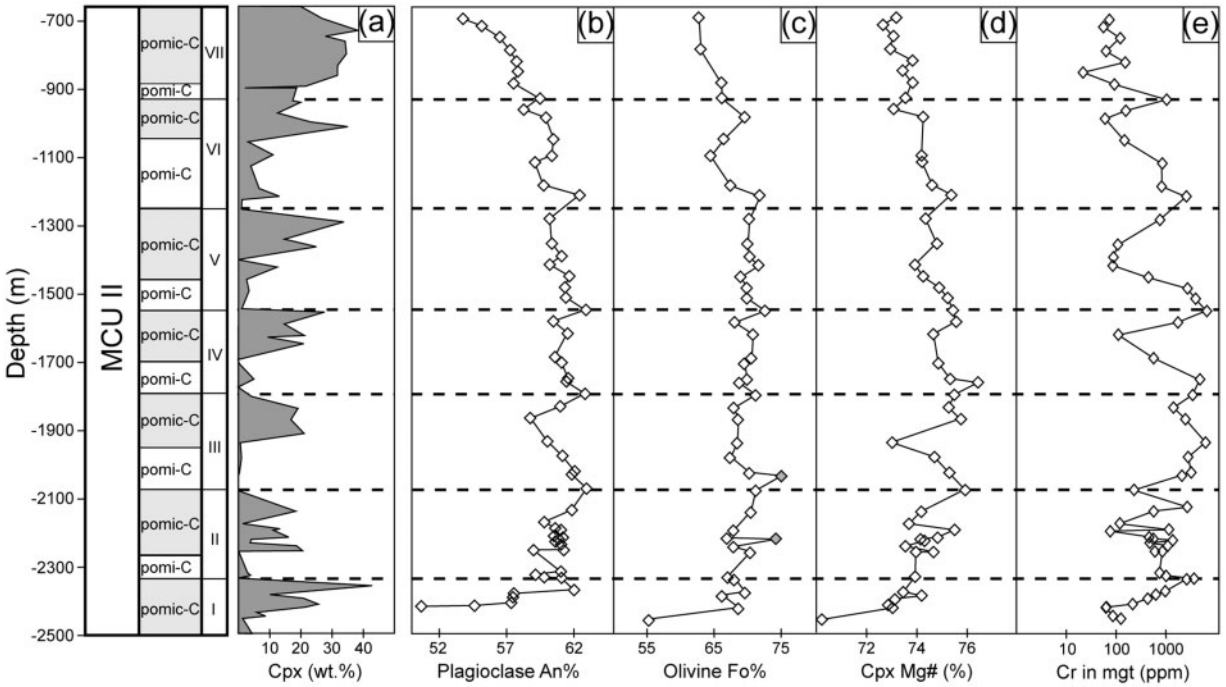

Fig. 13. Modal and compositional stratigraphic variations in the lower part of MCU II (from −2500 to −700 m). (a) Mineral mode of Ca-rich pyroxene; (b) An content of plagioclase; (c) Fo content of olivine; (d) Mg-number of Ca-rich pyroxene; (e) Cr content of magnetite. I–VII represent the seven cyclic units of MCU II (see text for explanation). Dashed lines represent the boundaries between cyclic units. The two grey diamonds in the olivine trend are samples that are interpreted to have undergone intense sub-solidus re-equilibration.

CONCLUSIONS

Modes and compositions of plagioclase, olivine, Ca-rich pyroxene and magnetite, as well as the Sr-isotope compositions of plagioclase separates and whole-rock data from the Sept Iles layered series allow us to reach the following conclusions.

(1) The Sept Iles layered intrusion crystallized from a ferrobasaltic parent magma. This magma was relatively close in composition to the parent magma of the Skaergaard intrusion (Hoover, 1989a; Toplis & Carroll, 1995; Nielsen, 2004; Thy et al., 2006) and typical ferrobasaltic lavas (Carmichael, 1964; Stout & Nicholls, 1977; Turner et al., 1992; Geist et al., 1995; Whitaker et al., 2008), except that it is much more enriched in FeO_t (*c.* 15 wt %) and TiO_2 (*c.* 3 wt %). The sequence of crystallization in the Sept Iles layered series is: plagioclase and olivine, followed by magnetite and ilmenite, then Ca-rich pyroxene and finally apatite. Examination of phase equilibria in ferrobasalt systems (Snyder et al., 1993; Toplis & Carroll, 1995; Botcharnikov et al., 2008) suggests that this sequence of crystallization is controlled by the parental magma composition, particularly its high FeO_t and TiO_2 contents and its low CaO content, which are responsible for the early saturation of Fe–Ti oxides, before that of Ca-rich pyroxene.

(2) Mineral modes display cyclicity in the layered series; this is particularly well illustrated by the presence of two apatite-rich layers, one in the middle and the other in the upper part of the layered series. Three megacyclic units (MCU) have thus been identified in the layered series. Each MCU shows the same succession of cumulus assemblages.

(3) MCU I displays a normal and uninterrupted differentiation trend of mineral evolution similar to that observed in smaller layered mafic igneous complexes, such as Skaergaard (McBirney, 1996) and Kiglapait (Morse, 1969). This differentiation trend is interrupted upwards by two large and many small reversals in mineral composition, resulting from magma chamber replenishment by undifferentiated primitive basaltic magma (Fig. 14). Intense mixing between the newly injected and resident magma must have occurred to account for the gradual evolution of mineral compositions in reversals. Disappearance of apatite, Ca-rich pyroxene and locally Fe–Ti oxides is associated with these magma chamber replenishments. The most evolved mineral compositions of the Sept Iles layered series are observed at the top of MCU II.

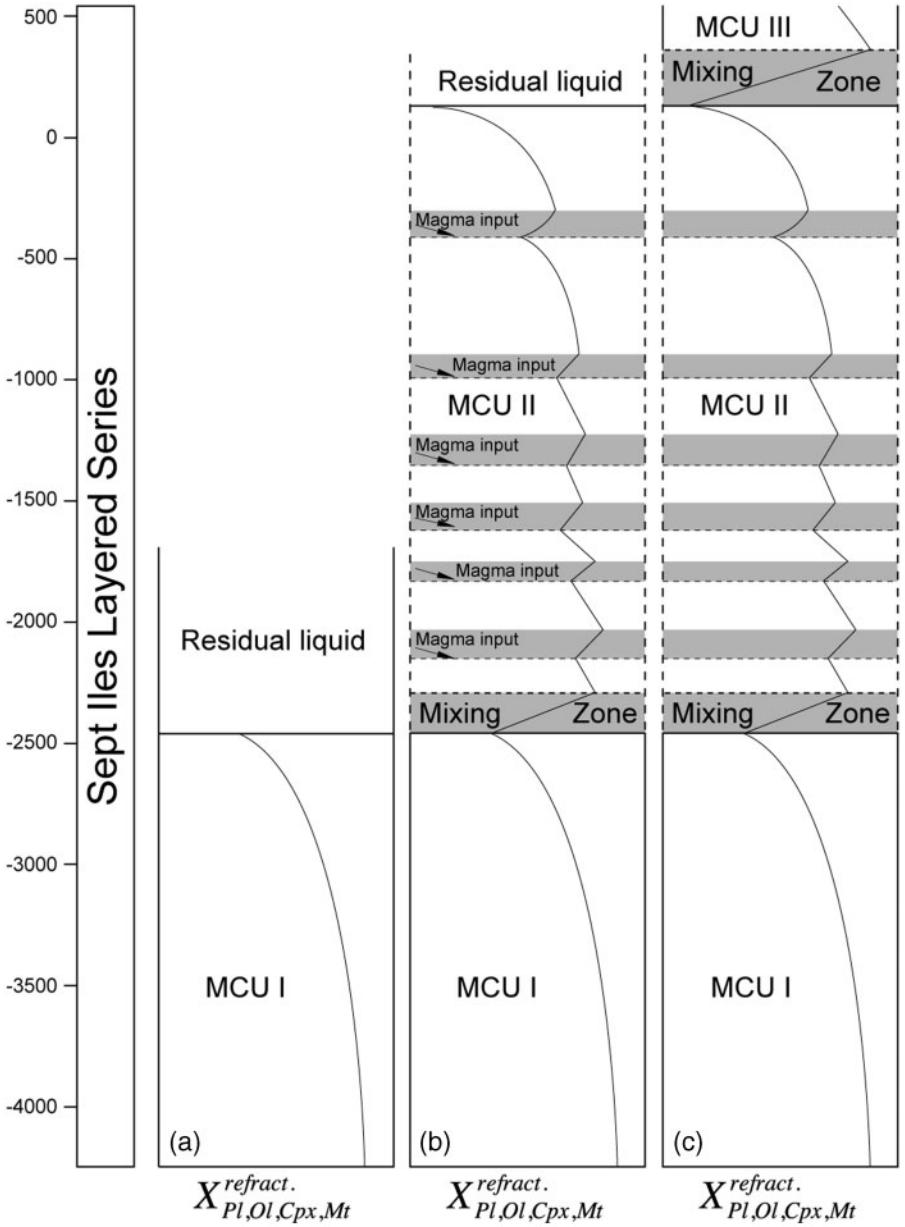

Fig. 14. Schematic model of magma chamber replenishments in the Sept Iles layered intrusion. (a) Crystallization of MCU I with a theoretical curve of mineral composition evolution and an arbitrary proportion of residual liquid left after the crystallization of MCU I. (b) Open-system crystallization of MCU II and theoretical curve of mineral composition evolution. MCU II starts by mixing between the residual resident magma of MCU I and a newly injected magma (mixing zone). Six significant magma inputs have occurred during the crystallization of MCU II and led mineral to more primitive compositions. An arbitrary proportion of residual liquid left after the crystallization of MCU II isindicated, which is lower than that left behind after the crystallization of MCU I (more evolved mineral compositions are reached at the end of MCU II). (c) Crystallization of MCU III, which starts by mixing with the resident magma after crystallization of MCU II. Evolved mineral compositions within MCU III are located below the St. Lawrence River and do not crop out.

ACKNOWLEDGEMENTS

This work was financed by the Belgian Fund for Joint Research (FNRS) and the Fund for Research in Industry and Agriculture (FRIA). M.D.H. would like to thank NSERC (Canada) for continuing Discovery grants. The Ministère des Ressources Naturelles et de la Faune du Québec is gratefully acknowledged for giving access to the drill-cores. G. Bologne, H. J. Bernhardt, C. Gilson and C. Pirard are thanked for the assistance with X-ray fluorescence, microprobe, Sr-isotopic and laser ablation inductively coupled plasma mass spectrometry (LA-ICP-MS)

analyses. We thank J. C. Duchesne for comments and discussions. Constructive reviews by A. R. McBirney and an anonymous reviewer were greatly appreciated.

SUPPLEMENTARY DATA

Supplementary data for this paper are available at *Journal of Petrology* online.

REFERENCES

Aigner-Torres, M., Blundy, J., Ulmer, P. & Pettke, T. (2007). Laser ablation ICPMS study of trace element partitioning between plagioclase and basaltic melts: An experimental approach. *Contributions to Mineralogy and Petrology* **153**, 647–667.

Amelin, Y., Heaman, L., Verchogliad, V. & Skobelev, V. (1994). Geochronological constraints on the emplacement history of an anorthosite–rapakivi granite suite—U–Pb zircon and baddeleyite study of the Korosten Complex, Ukraine. *Contributions to Mineralogy and Petrology* **116**, 411–419.

Andersen, D., Lindsley, D. & Davidson, P. (1993). Quilf—a Pascal program to assess equilibria among Fe–Mg–Mn–Ti oxides, pyroxenes, olivine, and quartz. *Computers and Geosciences* **19**, 1333–1350.

Beattie, P. (1994). Systematics and energetics of trace-element partitioning between olivine and silicate melts—implications for the nature of mineral melt partitioning. *Chemical Geology* **117**, 57–71.

Beike, D. K. & Rozgonyi, T. G. (1990). Mining the Dufek intrusion: Engineering and economic factors. *Geotechnical and Geological Engineering* **8**, 67–77.

Berndt, J., Koepke, J. & Holtz, F. (2005). An experimental investigation of the influence of water and oxygen fugacity on differentiation of MORB at 200 MPa. *Journal of Petrology* **46**, 135–167.

Bichan, R. (1970). The evolution and structural setting of the Great Dyke, Rhodesia. In: Clifford, T. N. & Gass, I. G. (eds) *African Magmatism and Tectonics*. Edinburgh: Oliver & Boyd, pp. 51–71.

Bindeman, I. N., Davis, A. M. & Drake, M. J. (1998). Ion microprobe study of plagioclase–basalt partition experiments at natural concentration levels of trace elements. *Geochimica et Cosmochimica Acta* **62**, 1175–1193.

Blundy, J. (1997). Experimental study of a Kiglapait marginal rock and implications for trace element partitioning in layered intrusions. *Chemical Geology* **141**, 73–92.

Bonin, B. (2007). A-type granites and related rocks: Evolution of a concept, problems and prospects. *Lithos* **97**, 1–29.

Botcharnikov, R. E., Almeev, R. R., Koepke, J. & Holtz, F. (2008). Phase relations and liquid lines of descent in hydrous ferrobasalt—implications for the Skaergaard intrusion and Columbia River flood basalts. *Journal of Petrology* **49**, 1687–1727.

Bougault, H. & Hekinian, R. (1974). Rift valley in the Atlantic Ocean near 36°50'N: Petrology and geochemistry of basalt rocks. *Earth and Planetary Science Letters* **24**, 249–261.

Brewer, T. S., Rex, D., Guise, P. G. & Hawkesworth, C. J. (1996). Geochronology of Mesozoic tholeiitic magmatism in Antarctica: Implications for the development of the failed Weddell Sea rift system. In: Storey, B. C., King, E. C. & Livermore, R. A. (eds) *Weddell Sea Tectonics and Gondwana Break-up. Geological Society, London, Special Publications* **108**, 45–61.

Brooks, C. K. & Nielsen, T. F. (1990). The differentiation of the Skaergaard intrusion: A discussion of Hunter and Sparks (*Contributions to Mineralogy and Petrology* 95, 451–461). *Contributions to Mineralogy and Petrology* **104**, 244–247.

Butcher, A. R., Pirrie, D., Prichard, H. M. & Fisher, P. (1999). Platinum-group mineralization in the Rum layered intrusion, Scottish Hebrides, UK. *Journal of the Geological Society, London* **156**, 213–216.

Byerly, G. R. (1980). The nature of differentiation trends in some volcanic rocks from the Galapagos Spreading Center. *Journal of Geophysical Research* **85**, 3797–3810.

Byerly, G. R., Melson, W. G. & Vogt, P. R. (1976). Rhyodacites, andesites, ferro-basalts and ocean tholeiites from the Galapagos Spreading Cente. *Earth and Planetary Science Letters* **30**, 215–221.

Cameron, E. N. (1978). The lower zone of the Eastern Bushveld Complex in Olifants River Trough. *Journal of Petrology* **19**, 437–462.

Cameron, E. N. (1980). Evolution of the lower critical zone, central sector, eastern Bushveld Complex, and its chromite deposits. *Economic Geology* **75**, 845–871.

Campbell, I. H. & Turner, J. S. (1986). The influence of viscosity on fountains in magma chambers. *Journal of Petrology* **27**, 1–30.

Campbell, I. H. & Turner, J. S. (1989). Fountains in magma chambers. *Journal of Petrology* **30**, 885–923.

Carmichael, I. S. (1964). The petrology of the Thingmuli, a Tertiary volcano in eastern Iceland. *Journal of Petrology* **5**, 435–460.

Cawthorn, R. G. (1996). Layered Intrusions. *Developments in Petrology* **15**, 544 pp.

Cawthorn, R. G. & Ashwal, L. D. (2009). Origin of anorthosite and magnetitite layers in the Bushveld Complex, constrained by major element compositions of plagioclase. *Journal of Petrology* **50**, 1607–1637.

Cawthorn, R. G. & McCarthy, T. S. (1980). Variations in Cr content of magnetite from the upper zone of the Bushveld Complex. Evidence for heterogeneity and convection currents in magma chambers. *Earth and Planetary Science Letters* **46**, 335–343.

Cawthorn, R. G., Meyer, P. S. & Kruger, F. J. (1991). Major addition of magma at the Pyroxenite Marker in the western Bushveld Complex, South Africa. *Journal of Petrology* **32**, 739–763.

Charlier, B., Skår, Ø., Korneliussen, A., Duchesne, J. C. & Vander Auwera, J. (2007). Ilmenite composition in the Tellnes Fe–Ti deposit, SW Norway: Fractional crystallization, postcumulus evolution and ilmenite–zircon relation. *Contributions to Mineralogy and Petrology* **154**, 119–134.

Cimon, J. (1998). *Le Complexe de Sept-Îles: I—L'Unité à apatite de Rivière des Rapides, Complexe de Sept-Îles; localisation stratigraphique et facteurs à l'origine de sa formation*. Quebec: Ministère de l'Energie et des Ressources du Québec, pp. 1–33.

Danyushevsky, L., Perfit, M., Eggins, S. & Falloon, T. (2003). Crustal origin for coupled 'ultra-depleted' and 'plagioclase' signatures in MORB olivine-hosted melt inclusions: Evidence from the Siqueiros Transform Fault, East Pacific Rise. *Contributions to Mineralogy and Petrology* **144**, 619–637.

Davidson, A. (1984). Identification of ductile shear zones in the southwestern Grenville Province of the Canadian Shield. In: Kröner, A. A. & Greiling, R. (eds) *Precambrian Tectonics Illustrated*. Stuttgart: Schweitzerbart, pp. 263–279.

Davidson, A. (1995). A review of the Grenville orogen in its North American type area. *Journal of Australian Geology and Geophysics* **16**, 3–24.

Davies, G. & Cawthorn, R. G. (1984). Mineralogical data on a multiple intrusion in the Rustenburg layered suite of the Bushveld Complex. *Mineralogical Magazine* **48**, 469–480.

Davies, G., Cawthorn, R. G., Barton, J. M. & Morton, M. (1980). Parental magma to the Bushveld Complex. *Nature* **287**, 33–35.

Day, J., Pearson, D. & Hulbert, L. (2008). Rhenium–osmium isotope and platinum-group element constraints on the origin and

evolution of the 1·27 Ga Muskox layered intrusion. *Journal of Petrology* **49**, 1255–1295.

Deckart, K., Bertrand, H. & Liegeois, J.P. (2005). Geochemistry and Sr, Nd, Pb isotopic composition of the Central Atlantic Magmatic Province (CAMP) in Guyana and Guinea. *Lithos* **82**, 289–314.

DePaolo, D. J. (1981). Trace element and isotopic effects of combined wallrock assimilation and fractional crystallization. *Earth and Planetary Science Letters* **53**, 189–202.

DePaolo, D. J. (1985). Isotopic studies of processes in mafic magma chambers. I. The Kiglapait Intrusion, Labrador. *Journal of Petrology* **26**, 925–951.

DePaolo, D. J. & Wasserburg, G. J. (1979). Petrogenetic mixing models and Nd–Sr isotopic patterns. *Geochimica et Cosmochimica Acta* **43**, 615–627.

Dion, D. J., Authier, K., Cimon, J. & Feininger, T. (1998). *Le complexe de Sept-Îles: II—Interpretation gravimétrique du complexe mafique stratifié de Sept-Îles*. Quebec: Ministère de l'Energie et des Ressources du Québec, pp. 33–41.

Doig, R. (1970). An alkaline rock province linking Europe and North America. *Canadian Journal of Earth Sciences* **7**, 22–28.

Doig, R. & Barton, J. M. (1968). Age of carbonatites and other alkaline rocks in Quebec. *Canadian Journal of Earth Sciences* **5**, 1401–1407.

Duchesne, J. C. (1999). Fe–Ti deposits in Rogaland anorthosites (South Norway): Geochemical characteristics and problems of interpretation. *Mineralium Deposita* **34**, 182–198.

Duchesne, J. C. & Bologne, G. (2009). XRF major and trace element determination in Fe–Ti oxide minerals. *Geologica Belgica* **12**, 205–212.

Duchesne, J. C. & Charlier, B. (2005). Geochemistry of cumulates from the Bjerkreim–Sokndal layered intrusion (S. Norway). Part I: Constraints from major elements on the mechanism of cumulate formation and on the jotunite liquid line of descent. *Lithos* **83**, 229–254.

Duchesne, J. C. & Hertogen, J. (1988). Le magma parental du lopolithe de Bjerkreim–Sokndal (Norvège méridionale). *Comptes Rendus de l'Académie des Sciences* **306**, 45–48.

Duchesne, J. C. & Wilmart, E. (1997). Igneous charnockites and related rocks from the Bjerkreim–Sokndal layered intrusion (Southwest Norway): a jotunite (hypersthene monzodiorite)-derived A-type granitoid suite. *Journal of Petrology* **38**, 337–369.

Duchesne, J. C., Shumlyanskyy, L. & Charlier, B. (2006). The Fedorivka layered intrusion (Korosten Pluton, Ukraine): An example of highly differentiated ferrobasaltic evolution. *Lithos* **89**, 353–376.

Eales, H. V. & Cawthorn, R. G. (1996). The Bushveld Complex. In: Cawthorn, R. G. (ed.) *Layered Intrusions. Developments in Petrology* **15**, 181–230.

Eaton, D., Hynes, A., Indares, A. & Rivers, T. (1995). Seismic images of eclogites, crustal-scale extension, and moho relief in the Eastern Grenville Province, Quebec. *Geology* **23**, 855–858.

Eggins, S. M., Rudnick, R. L. & McDonough, W. F. (1998). The composition of peridotites and their minerals: A laser-ablation ICP-MS study. *Earth and Planetary Science Letters* **154**, 53–71.

Emeleus, C. H., Cheadle, M. J., Hunter, R. H., Upton, B. J. & Wadsworth, W. J. (1996). The Rum layered suite. In: Cawthorn, R. G. (ed.) *Layered Intrusions. Developments in Petrology* **15**, 403–439.

Ewart, A. & Griffin, W. L. (1994). Application of proton-microprobe data to trace-element partitioning in volcanic rocks. *Chemical Geology* **117**, 251–284.

Falloon, T. J., Green, D. H., Danyushevsky, L. V. & Faul, U. H. (1999). Peridotite melting at 1·0 and 1·5 GPa: An experimental evaluation of techniques using diamond aggregates and mineral mixes for determination of near-solidus melts. *Journal of Petrology* **40**, 1343–1375.

Feig, S., Koepke, J. R. & Snow, J. (2006). Effect of water on tholeiitic basalt phase equilibria: An experimental study under oxidizing conditions. *Contributions to Mineralogy and Petrology* **152**, 611–638.

Ferris, J., Johnson, A. & Storey, B. (1998). Form and extent of the Dufek intrusion, Antarctica, from newly compiled aeromagnetic data. *Earth and Planetary Science Letters* **154**, 185–202.

Forsyth, D., Milkereit, B., Zelt, C., White, D., Easton, R. & Hutchinson, D. (1994). Deep-structure beneath Lake-Ontario—crustal-scale Grenville subdivisions. *Canadian Journal of Earth Sciences* **31**, 255–270.

Geist, D., Howard, K. A. & Larson, P. (1995). The generation of oceanic rhyolites by crystal fractionation: The basalt–rhyolite association at Volcán Alcedo, Galápagos Archipelago. *Journal of Petrology* **36**, 965–982.

Ghiorso, M. S. & Sack, R. O. (1995). Chemical mass transfer in magmatic processes. IV. A revised and internally consistent thermodynamic model for the interpolation and extrapolation of liquid–solid equilibria in magmatic systems at elevated temperatures and pressures. *Contributions to Mineralogy and Petrology* **119**, 197–212.

Green, A. G., Milkereit, B., Davidson, A., Spencer, C., Hutchinson, D. R., Cannin, W. F., Lee, M. W., Agena, W. F., Behrendt, J. C. & Hinze, W. J. (1988). Crustal structure of the Grenville Front and adjacent terranes. *Geology* **16**, 788–792.

Green, D. H., Hibberson, W. O. & Jaques, A. L. (1979). Petrogenesis of mid-ocean ridge basalts. In: McElhinney, M. W. (ed.) *The Earth: Its Origin, Structure and Evolution*. London: Academic Press, pp. 265–299.

Hamilton, J. (1977). Strontium isotopes and trace element studies on the Great Dyke and Bushveld mafic phase and their relation to early Proterozoic magma genesis in southern Africa. *Journal of Petrology* **18**, 24–52.

Hart, S. & Dunn, T. (1993). Experimental cpx melt partitioning of 24 trace-elements. *Contributions to Mineralogy and Petrology* **113**, 1–8.

Hatton, C. J. (1984). The effect of pressure, temperature and composition on the distribution of Fe and Mg between olivine, orthopyroxene and liquid: An appraisal of the reversal in the normal fractionation trend in the Bushveld Complex. *Contributions to Mineralogy and Petrology* **86**, 45–53.

Higgins, M. D. (2005). A new model for the structure of the Sept Iles Intrusive suite, Canada. *Lithos* **83**, 199–213.

Higgins, M. D. & Doig, R. (1977). 540 Myr-old anorthosite complex in the Grenville province of Quebec, Canada. *Nature* **267**, 40–41.

Higgins, M. D. & Doig, R. (1981). The Sept Iles anorthosite complex: Field relationships, geochronology and petrology. *Canadian Journal of Earth Sciences* **18**, 561–573.

Higgins, M. D. & Doig, R. (1986). Geochemical constraints on the processes that were active in the Sept Iles complex. *Canadian Journal of Earth Sciences* **23**, 670–681.

Higgins, M. D. & van Breemen, O. (1998). The age of the Sept Iles layered mafic intrusion, Canada: Implications for the Late Neoproterozoic/Cambrian history of Southeastern Canada. *Journal of Geology* **106**, 421–431.

Hill, R. I., Campbell, I. H., Davies, G. & Griffiths, R. W. (1992). Mantle plumes and continental tectonics. *Science* **256**, 186–193.

Himmelberg, G. R. & Ford, A. B. (1977). Iron–titanium oxides of the Dufek intrusion, Antarctica. *American Mineralogist* **62**, 623–633.

Hirschmann, M. M. (1992). Origin of the transgressive granophyres from the layered series of the Skaergaard intrusion, East Greenland. *Journal of Volcanology and Geothermal Research* **52**, 185–207.

Hirschmann, M. M., Renne, P. R. & McBirney, A. R. (1997). $^{40}Ar/^{39}Ar$ dating of the Skaergaard Intrusion. *Earth and Planetary Science Letters* **146**, 645–658.

Holness, M. B., Tegner, C., Nielsen, T. F., Stripp, G. & Morse, S. A. (2007*a*). A textural record of solidification and cooling in the Skaergaard intrusion, East Greenland. *Journal of Petrology* **48**, 2359–2377.

Holness, M. B., Nielsen, T. F. & Tegner, C. (2007*b*). Textural maturity of cumulates: A record of chamber filling, liquidus assemblage, cooling rate and large-scale convection in mafic layered intrusions. *Journal of Petrology* **48**, 141–157.

Hoover, J. D. (1989*a*). The chilled marginal gabbro and other contact rocks of the Skaergaard intrusion. *Journal of Petrology* **30**, 441–476.

Hoover, J. D. (1989*b*). Petrology of the Marginal Border Series of the Skaergaard intrusion. *Journal of Petrology* **30**, 399–439.

Hunter, R. H. & Sparks, R. S. (1987). The differentiation of the Skaergaard intrusion. *Contributions to Mineralogy and Petrology* **95**, 451–461.

Irvine, T. N. (1975). Crystallization sequences in the Muskox intrusion and other layered intrusions—II. Origin of chromitite layers and similar deposits of other magmatic ores. *Geochimica et Cosmochimica Acta* **39**, 991–1020.

Irvine, T. N. (1982). Terminology for layered intrusions. *Journal of Petrology* **23**, 127–162.

Irvine, T. N., Keith, D. W. & Todd, S. G. (1983). The J-M platinum–palladium reef of the Stillwater Complex, Montana. II. Origin of double-diffusive convective magma mixing and implications for the Bushveld Complex. *Economic Geology* **78**, 1287–1334.

Jang, Y. D., Naslund, H. R. & McBirney, A. R. (2001). The differentiation trend of the Skaergaard intrusion and the timing of magnetite crystallization: Iron enrichment revisited. *Earth and Planetary Science Letters* **189**, 189–196.

Jensen, J. C., Nielsen, F. M., Duchesne, J. C., Demaiffe, D. & Wilson, J. R. (1993). Magma influx and mixing in the Bjerkreim–Sokndal layered intrusion, South Norway: Evidence from the boundary between two megacyclic units at Storeknuten. *Lithos* **29**, 311–325.

Juster, T. C., Grove, T. L. & Perfit, M. R. (1989). Experimental constraints on the generation of FeTi basalts, andesites, and rhyodacites at the Galapagos Spreading Center, 85°W and 95°W. *Journal of Geophysical Research* **94**, 9251–9274.

Kamo, S. L., Gower, C. F. & Krogh, T. E. (1989). Birthdate for the Iapetus Ocean? A precise U–Pb zircon and baddeleyite age for the Lang Range Dykes, southeast Labrador. *Geology* **17**, 602–605.

Kleeman, G. J. & Twist, D. (1989). The compositionally-zoned sheet-like granite pluton of the Bushveld Complex: Evidence bearing on the nature of A-type magmatism. *Journal of Petrology* **30**, 1383–1414.

Klemm, D. D., Henckel, J., Dehm, R. & von Gruenewaldt, G. (1985). The geochemistry of titanomagnetite in magnetite layers and their host rocks of the Eastern Bushveld Complex. *Economic Geology* **80**, 1075–1088.

Klemme, S., Gunther, D., Hametner, K., Prowatke, S. & Zack, T. (2006). The partitioning of trace elements between ilmenite, ulvöspinel, armalcolite and silicate melts with implications for the early differentiation of the moon. *Chemical Geology* **234**, 251–263.

Klewin, K. W. (1990). Petrology of the Proterozoic Potato River layered intrusion, Northern Wisconsin, USA. *Journal of Petrology* **31**, 1115–1139.

Kolker, A. (1982). Mineralogy and geochemistry of Fe–Ti oxide and apatite (nelsonite) deposits and evaluation of the liquid immiscibility hypothesis. *Economic Geology* **77**, 1146–1148.

Kress, V. C. & Carmichael, I. S. (1991). The compressibility of silicate liquids containing Fe_2O_3 and the effect of composition, temperature, oxygen fugacity and pressure on their redox states. *Contributions to Mineralogy and Petrology* **108**, 82–92.

Kruger, F. (2005). Filling the Bushveld Complex magma chamber: Lateral expansion, roof and floor interaction, magmatic unconformities, and the formation of giant chromitite, PGE and Ti–V–magnetitite deposits. *Mineralium Deposita* **40**, 451–472.

Kumarapeli, P. S. (1993). A plume-related segment in the rifted margin of Laurentia, southern Canadian Appalachians, seen through a completed Wilson cycle. *Tectonophysics* **219**, 47–55.

Kumarapeli, P. S. & Saull, V. A. (1966). The St-Lawrence Valley system: A North American equivalent of the East African rift system. *Canadian Journal of Earth Sciences* **3**, 639–657.

Larson, S. A., Hogmalm, K. J. & Meurer, W. P. (2008). Character and significance of spectacular layering features developed in the thin, alkali-basaltic sills of the Ulvö Gabbro Complex, Sweden. *Mineralogy and Petrology* **92**, 427–452.

LeCheminant, A. N. & Heaman, L. (1989). Mackenzie igneous events, Canada: Middle Proterozoic hotspot magmatism associated with ocean opening. *Earth and Planetary Science Letters* **96**, 38–48.

Lee, C. A. (1996). A review of mineralizations in the Bushveld Complex and some other layered mafic intrusions. In: Cawthorn, R. G. (ed.) *Layered Intrusions. Developments in Petrology* **15**, 103–146.

Leeman, W. P., Ma, M. S., Murali, A. V. & Schmitt, R. A. (1978). Empirical estimation of the magnetite/liquid distribution coefficients for some transition elements. *Contributions to Mineralogy and Petrology* **65**, 269–272.

Loncarevic, B. D., Feininger, T. & Lefebvre, D. (1990). The Sept-Iles layered mafic intrusion: Geophysical expression. *Canadian Journal of Earth Sciences* **27**, 501–512.

Mathison, C. I. & Ahmat, A. L. (1996). The Windimurra Complex, Western Australia. In: Cawthorn, R. G. (ed.) *Layered Intrusions. Developments in Petrology* **15**, 485–510.

Mathison, C. I. & Hamlyn, P. R. (1987). The McIntosh layered troctolite–olivine gabbro intrusion, East Kimberley, Western Australia. *Journal of Petrology* **28**, 211–234.

McBirney, A. R. (1989). The Skaergaard layered series: I. Structure and average compositions. *Journal of Petrology* **30**, 363–399.

McBirney, A. R. (1996). The Skaergaard intrusion. In: Cawthorn, R. G. (ed.) *Layered Intrusions. Developments in Petrology* **15**, 147–180.

McBirney, A. R. & Hunter, R. H. (1995). The cumulus paradigm reconsidered. *Journal of Geology* **103**, 114–122.

McBirney, A. R. & Naslund, H. R. (1990). The differentiation of the Skaergaard intrusion: A discussion of Hunter and Sparks (*Contributions to Mineralogy and Petrology* 95, 451–461). *Contributions to Mineralogy and Petrology* **104**, 235–240.

McBirney, A. R. & Noyes, R. M. (1979). Crystallization and layering of the Skaergaard intrusion. *Journal of Petrology* **20**, 487–554.

McCallum, I. S. (1996). The Stillwater Complex. In: Cawthorn, R. G. (ed.) *Layered Intrusions. Developments in Petrology* **15**, 441–484.

McCarthy, T. S. & Cawthorn, R. G. (1983). The geochemistry of vanadiferous magnetite in the Bushveld Complex: Implications for crystallization mechanisms in layered complexes. *Mineralium Deposita* **18**, 505–518.

McNeill, A. W. & Danyushevsky, L. (1996). Composition and crystallization temperatures of primary melts from Hole 896A basalts: Evidence from melt inclusion studies. In: Alt, J. C., Kinoshota, H., Stokking, L. B. & Michael, P. J. (eds) *Proceedings of the Ocean Drilling Program: Scientific Results, 148*. College Station, TX: Ocean Drilling Program, pp. 21–35.

Means, W. D. & Park, Y. (1994). New experimental approach to understanding igneous texture. *Geology* **22**, 323–326.

Meurer, W. P. & Boudreau, A. E. (1996). Petrology and mineral compositions of the middle banded series of the Stillwater Complex, Montana. *Journal of Petrology* **37**, 583–607.

Miller, J. D. & Ripley, E. M. (1996). Layered intrusions of the Duluth Complex, USA. In: Cawthorn, R. G. (ed.) *Layered Intrusions. Developments in Petrology* **15**, 257–301.

Mitchell, A. A., Eales, H. V. & Kruger, F. J. (1998). Magma replenishment, and the significance of poikilitic textures, in the Lower Main Zone of the western Bushveld Complex, South Africa. *Mineralogical Magazine* **62**, 435–450.

Morse, S. A. (1969). *The Kiglapait Layered Intrusion, Labrador. Geological Society of America, Memoirs* **112**, 204 pp.

Morse, S. A. (1979). Kiglapait geochemistry II: petrography. *Journal of Petrology* **20**, 591–624.

Morse, S. A. (1990). The differentiation of the Skaergaard intrusion: A discussion of Hunter and Sparks (*Contributions to Mineralogy and Petrology* 95, 451–461). *Contributions to Mineralogy and Petrology* **104**, 240–244.

Morse, S. A. & Ross, M. (2004). Kiglapait mineralogy IV: The augite series. *American Mineralogist* **89**, 1380–1395.

Morse, S. A., Young, I. M. & Ball, S. S. (1981). Xenoliths in the Kiglapait intrusion. In: Morse, S. A. (ed.) *Nain anorthosite project, Labrador: Field report 1981. University of Massachusetts Geological, Geographical Departments Contributions* **40**, 87–94.

Musset, A. E., Dagley, P. & Skelhorn, R. R. (1988). Time and duration of activity in the British Tertiary Igneous Province. In: Morton, A. C. & Parson, L. M. (eds) *Early Tertiary Volcanism and the Opening of the North Atlantic. Geological Society, London, Special Publications* **39**, 337–348.

Namur, O., Charlier, B., Higgins, M. D. & Vander Auwera, J. (2007). The Sept Iles Mafic Layered Intrusion: An example of ferrobasaltic differentiation. Goldschmidt Geochemistry, Cologne, Germany. *Geochimica et Cosmochimica Acta* **71**, 705.

Naslund, H. R. (1989). Petrology of the Basistoppen Sill, East Greenland: A calculated magma differentiation trend. *Journal of Petrology* **30**, 299–319.

Nielsen, T. F. (2004). The shape and volume of the Skaergaard intrusion, Greenland: Implications for mass balance and bulk composition. *Journal of Petrology* **45**, 507–530.

Nielsen, F. M., Campbell, I. H., McCulloch, M. & Wilson, J. R. (1996). A strontium isotopic investigation of the Bjerkreim–Sokndal layered intrusion, Southwest Norway. *Journal of Petrology* **37**, 171–193.

Nolan, K. M. & Morse, S. A. (1986). Marginal rocks resembling the estimated bulk composition of the Kiglapait Intrusion. *Geochimica et Cosmochimica Acta* **50**, 2381–2386.

O'Neill, H. S. (1987). Quartz–fayalite–iron and quartz–fayalite–magnetite equilibria in the free energy of formation of fayalite (Fe_2SiO_4) and magnetite (Fe_3O_4). *American Mineralogist* **72**, 67–75.

Osborn, E. F. (1980). On the cause of the reversal of the normal fractionation trend—an addendum to the paper by E. N. Cameron, 'Evolution of the lower critical zone, central sector, eastern Bushveld Complex, and its chromite deposits'. *Economic Geology* **75**, 872–875.

Paces, J. B. & Miller, J. D. (1993). Precise U–Pb ages of Duluth Complex and related mafic intrusions, Northeastern Minnesota—geochronological insights to physical, petrogenetic, paleomagnetic, and tectonomagmatic processes associated with the 1·1 Ga midcontinent rift system. *Journal of Geophysical Research—Solid Earth* **98**, 13997–14013.

Pang, K. N., Li, C., Zhou, M. F. & Ripley, E. M. (2009). Mineral compositional constraints on petrogenesis and oxide ore genesis of the late Permian Panzhihua layered gabbroic intrusion, SW China. *Lithos* **110**, 199–214.

Panjasawatwong, Y., Danyushevsky, L. V., Crawford, A. J. & Harris, K. L. (1995). An experimental study of the effects of melt composition on plagioclase–melt equilibria at 5 and 10 kbar: Implications for the origin of magmatic high-An plagioclase. *Contributions to Mineralogy and Petrology* **118**, 420–432.

Pearce, N. J., Perkins, W. T., Westgate, J. A., Gorton, M. P., Jackson, S. E., Neal, C. R. & Chenery, S. P. (1997). A compilation of new and published major and trace element data for NIST SRM 610 and NIST SRM 612 glass reference materials. *Geostandards Newsletter* **21**, 115–144.

Philpotts, A. R. (1967). Origin of certain iron–titanium oxide and apatite rocks. *Economic Geology* **62**, 303–315.

Reynolds, I. (1985). The nature and origin of titaniferous magnetite-rich layers in the Upper Zone of the Bushveld complex: A review and synthesis. *Economic Geology* **80**, 1089–1108.

Rivers, T., Martignole, J., Gower, C. F. & Davidson, A. (1989). New tectonic divisions of the Grenville Province, southeastern Canadian Shield. *Tectonics* **8**, 63–84.

Rivers, T., van Gool, J. A. & Connelly, J. N. (1993). Contrasting tectonic styles in the northern Grenville Province: Implications for dynamics of orogenic fronts. *Geology* **21**, 1127–1130.

Roeder, P. L. & Emslie, R. F. (1970). Olivine–liquid equilibrium. *Contributions to Mineralogy and Petrology* **29**, 275–289.

Schärer, U., Wilmart, E. & Duchesne, J. C. (1996). The short duration and anorogenic character of anorthosite magmatism: U–Pb dating from the Rogaland complex, Norway. *Earth and Planetary Science Letters* **139**, 335–350.

Shaw, D. H., Cramer, J. J., Higgins, M. D. & Truscott, M. G. (1986). Composition of the Canadian Precambrian shield and the continental crust of the Earth. In: Dawson, J. B., Carswell, D. A., Hall, J. & Wedepohl, K. H. (eds) *The Nature of the Lower Continental Crust. Geological Society, London, Special Publications* **24**, 275–282.

Simmons, K. R., Wiebe, R. A., Snyder, D. & Simmons, E. C. (1986). U–Pb zircon age for the Newark Island Layered Intrusion, Nain anorthosite complex, Labrado. *Geological Society of America, Abstracts with Programs* **18**, 751.

Snyder, D., Carmichael, I. S. & Wiebe, R. A. (1993). Experimental study of liquid evolution in an Fe-rich layered mafic intrusion: Constraints of Fe–Ti oxide precipitation on the T–fO_2 and T–ρ paths of tholeiitic magmas. *Contributions to Mineralogy and Petrology* **113**, 73–86.

Sonnenthal, E. L. & McBirney, A. R. (1998). The Skaergaard layered series. Part IV. Reaction-transport simulations of foundered blocks. *Journal of Petrology* **39**, 633–661.

Steiger, R. H. & Jäger, E. (1977). Subcommission on geochronology: Convention of the use of decay constants in geo- and cosmochronology. *Earth and Planetary Science Letters* **36**, 359–362.

Stormer, J. C. & Nicholls, J. (1978). XLFRAC: A program for the interactive testing of magmatic differentiation models. *Computers and Geosciences* **4**, 143–159.

Stout, M. Z. & Nicholls, J. (1977). Mineralogy and petrology of Quaternary lavas from the Snake River Plain, Idaho. *Canadian Journal of Earth Sciences* **14**, 2140–2156.

Sun, S. S. & McDonough, W. F. (1989). Chemical and isotopic systematics of oceanic basalts: Implication for mantle composition and process. In: Saunders, A. D. & Norry, M. J. (eds) *Magmatism in the Ocean Basins. Geological Society, London, Special Publications* **42**, 313–345.

Tegner, C., Cawthorn, R. G. & Kruger, F. J. (2006). Cyclicity in the Main and Upper Zones of the Bushveld Complex, South Africa: Crystallization from a zoned magma sheet. *Journal of Petrology* **47**, 2257–2279.

Thy, P. & Lofgren, G. E. (1994). Experimental constraints on the low-pressure evolution of transitional and midly alkalic basalts: The

effect of Fe–Ti oxide minerals and the origin of basaltic andesites. *Contributions to Mineralogy and Petrology* **116**, 340–351.

Thy, P., Lesher, C. E., Nielsen, T. F. & Brooks, C. K. (2006). Experimental constraints on the Skaergaard liquid line of descent. *Lithos* **92**, 154–180.

Thy, P., Lesher, C. E. & Tegner, C. (2009). The Skaergaard liquid line of descent revisited. *Contributions to Mineralogy and Petrology* **157**, 735–747.

Tollari, N., Barnes, S. J., Cox, R. A. & Nabil, H. (2008). Trace element concentrations in apatites from the Sept-Iles Intrusive Suite, Canada—Implications for the genesis of nelsonites. *Chemical Geology* **252**, 180–190.

Toplis, M. J. (2005). The thermodynamics of iron and magnesium partitioning between olivine and liquid: Criteria for assessing and predicting equilibrium in natural and experimental systems. *Contributions to Mineralogy and Petrology* **149**, 22–39.

Toplis, M. J. & Carroll, M. R. (1995). An experimental study of the influence of oxygen fugacity on Fe–Ti oxide stability, phase relations, and mineral–melt equilibria in ferro-basaltic systems. *Journal of Petrology* **36**, 1137–1170.

Toplis, M. J. & Corgne, A. (2002). An experimental study of element partitioning between magnetite, clinopyroxene and iron-bearing liquids with particular emphasis on vanadium. *Contributions to Mineralogy and Petrology* **144**, 22–37.

Toplis, M. J., Libourel, G. & Carroll, M. R. (1994). The role of phosphorus in crystallization processes of basalt: An experimental study. *Geochimica et Cosmochimica Acta* **58**, 797–810.

Turner, S. P., Foden, J. D. & Morrison, R. S. (1992). Derivation of some A-type magmas by fractionation of basaltic magma: An example from the Padthaway Ridge, South Australia. *Lithos* **28**, 151–179.

Vander Auwera, J. & Longhi, J. (1994). Experimental study of a jotunite (hypersthene monzodiorite): Constraints on the parent magma composition and crystallization conditions (P, T, fO_2) of the Bjerkreim–Sokndal layered intrusion (Norway). *Contributions to Mineralogy and Petrology* **118**, 60–78.

Vannucci, R., Bottazzi, P., Wulff-Pedersen, E. & Neumann, E. R. (1998). Partitioning of REE, Y, Sr, Zr and Ti between clinopyroxene and silicate melts in the mantle under La Palma (Canary Islands): Implications for the nature of the metasomatic agents. *Earth and Planetary Science Letters* **158**, 39–51.

Van Schmus, W. R., Green, J. C. & Halls, H. C. (1982). Geochronology of Keweenawan rocks of the Lake Superior region: A summary. In: Wold, R. J. & Hinze, W. J. (eds) *Geology and Tectonics of the Lake Superior Basin. Geological Society of America, Memoirs* **156**, 165–171.

Wadleigh, M. A., Veizer, J. & Brooks, C. (1985). Strontium and isotopes in Canadian rivers: Fluxes and global implications. *Geochimica et Cosmochimica Acta* **49**, 1727–1736.

Wager, L. R. & Brown, G. M. (1968). *Layered Igneous Rocks*. San Francisco, CA: W. H. Freeman, 588 p.

Walraven, F., Armstrong, R. A. & Kruger, F. J. (1990). A chronostratigraphic framework for the north–central Kaapvaal Craton, the Bushveld Complex and the Vredefort structure. *Tectonophysics* **171**, 23–48.

Whitaker, M. L., Nekvasil, H., Lindsley, D. & McCurry, M. (2008). Can crystallization of olivine tholeiite give rise to potassic rhyolites? An experimental investigation. *Bulletin of Volcanology* **70**, 417–434.

Wiebe, R. A. (1988). Structural and magmatic evolution of a magma chamber: The Newark Island layered intrusion, Nain, Labrador. *Journal of Petrology* **29**, 383–411.

Wiebe, R. A. & Snyder, D. (1993). Slow, dense replenishments of a basic magma chamber: The layered series of the Newark Island layered intrusion, Nain, Labrador. *Contributions to Mineralogy and Petrology* **113**, 59–72.

Wilson, A. H. (1982). The geology of the 'Great Dyke', Zimbabwe: The ultramafic rocks. *Journal of Petrology* **23**, 240–292.

Wilson, A. H. (1996). The Great Dyke of Zimbabwe. In: Cawthorn, R. G. (ed.) *Layered Intrusions. Developments in Petrology* **15**, 365–402.

Wilson, A. H. & Prendergast, M. D. (2001). Platinum-group element mineralisation in the Great Dyke, Zimbabwe, and its relationship to magma evolution and magma chamber structure. *South African Journal of Geology* **104**, 319–342.

Wilson, J. R. & Sorensen, H. S. (1996). The Fongen–Hyllingen layered intrusive complex. In: Cawthorn, R. G. (ed.) *Layered Intrusions. Developments in Petrology* **15**, 303–330.

Wilson, J. R., Hansen, B. & Pedersen, S. (1983). Zircon U–Pb evidence for the age of the Fongen–Hyllingen complex, Trondheim region, Norway. *Geologiska Foreningens i Stockholm Forhandlingar* **105**, 68–70.

Wilson, J. R., Robins, B., Nielsen, F. M., Duchesne, J. C. & Vander Auwera, J. (1996). The Bjerkreim–Sokndal layered intrusion, Southwest Norway. In: Cawthorn, R. G. (ed.) *Layered Intrusions. Developments in Petrology* **15**, 231–255.

Wynne-Edwards, H. R. (1972). The Grenville Province. In: Price, R. & Douglas, R. J. (eds) *Variations in Tectonic Styles in Canada. Geological Association of Canada, Special Papers* **11**, 263–334.

Zhou, M. F., Robinson, P. T., Lesher, C. M., Keays, R. R., Zhang, C. J. & Malpas, J. (2005). Geochemistry, petrogenesis and metallogenesis of the Panzhihua gabbroic layered intrusion and associated Fe–Ti–V oxide deposits, Sichuan Province, SW China. *Journal of Petrology* **46**, 2253–2280.

APPENDIX

Analytical methods

One hundred and eighty-seven cumulate samples and four fine-grained mafic samples were selected for geochemical analysis. All the samples (*c.* 2 kg) were carefully cleaned prior to crushing. They were manually crushed with a hammer and milled in agate mortars. Whole-rock compositions were obtained for major and some trace elements (Rb, Sr, Y, Zr, Nb, Co, Cu, Ga, Ni, Zn, Ba, Cr and V) by XRF using an ARL 9400XP spectrometer at the University of Liège (Belgium). Major elements were measured on lithium tetra- and meta-borate fused glass discs, with matrix corrections following the Traill–Lachance algorithm. Trace elements were measured on pressed powder pellets and data were corrected for matrix effects by Compton peak monitoring. Accuracy is estimated as better than 1% for major elements and 5% for trace elements, and was controlled using 40 international and in-house standards. Fe^{2+} was determined by titration with $K_2Cr_2O_7$.

One hundred and eighty samples were selected for plagioclase separation (80–150 μm) using flotation in bromoform and magnetic separation (Frantz isodynamic separator). Final purification was realized by HCl leaching of mineral separates to dissolve any grains of apatite,

followed by intense cleaning of the mineral powder in ultrapure water and grinding in an agate mortar. Major and trace (Sr, Ba) element compositions were obtained by XRF on Li-fused glass discs and pressed powder pellets respectively.

Olivine (125 samples), Ca-rich pyroxene (135 samples) and orthopyroxene (27 samples) compositions were obtained with a Cameca SX 50 electron microprobe at the University of Bochum (Germany). Analytical conditions were 15 kV for the accelerating voltage and 15 nA for the beam current. A focused beam of 2 μm diameter was used to avoid any problem resulting from the presence of inclusions. When possible, at least three points in the cores of three grains were measured and the values reported here correspond to the mean of all the measurements, which had a total between 98·5 and 101·5 wt %. The following standards were used for Kα X-ray lines calibration: andradite for Si, Fe and Ca; synthetic rutile for Ti; spessartine for Al and Mn; pyrope for Mg; jadeite for Na; and K-glass for K. Crystals used in spectrometers were TAP for Si, Mg and Al; PET for Ti, Ca, Na and K; and LIF for Mn and Fe. Raw data were corrected with the CATZAF software. The major element compositions of 26 Ca-rich pyroxene separates were determined by XRF on fused glass discs. Bulk compositions were compared with the average compositions of *in situ* electron microprobe analyses and differences were found to be negligible.

One hundred and sixty-one samples of magnetite were separated by hand-magnet and heavy liquids (bromoform and hot Clerici's solution). Chromium was analysed by XRF on pressed powder pellets following the method of Duchesne & Bologne (2009). International Fe–Ti oxide reference materials as well as synthetic and in-house standards were used for calibration. Accuracy was estimated as better than 5% and the detection limit was calculated at 50 ppm. Ten samples of ilmenite were separated by heavy liquids. Major element compositions of magnetite and ilmenite were determined in 10 samples by XRF on Li-fused glass discs, following the method of Duchesne & Bologne (2009).

Strontium isotope compositions were analysed on 20 samples of plagioclase separates and on one whole-rock powder of country rock (07-08), by thermal ionization mass spectrometry (TIMS) at the Royal Museum for Central Africa (Tervuren, Belgium). For dissolution, 0·05–0·17 g of fine-grained milled plagioclase and whole-rock were dissolved in a Teflon beaker using a mixture of distilled 29N HF and 14N HNO_3. The solutions were dried and taken up with 6N HCl. The purity of the dissolutions was carefully checked. The solutions were then dried and taken up with 2·5N HCl. From this solution, an aliquot of *c.* 3000 ng of Sr was weighed and dried. The aliquot was then taken up by 2 ml 2N HNO_3 and loaded into an ion exchange column. The Sr was eluded by 2 ml 0·05N HNO_3. A third of the Sr was loaded with phosphoric acid on a single outgassed Ta filament from the GV Sector 54 multi-collector mass spectrometer for measurement. Repeated measurements of Sr isotope ratios agreed at better than 0·000012. The standard NBS987 was used and gave a value of $0{\cdot}710286 \pm 0{\cdot}000005$ for $^{87}Sr/^{86}Sr$, with a normalization value of 0·1194 for $^{87}Sr/^{88}Sr$. The decay constant used was $1{\cdot}42 \times 10^{-11}\,a^{-1}$ for ^{87}Rb (Steiger & Jäger, 1977). Initial $^{87}Sr/^{86}Sr$ ratios were calculated for an age of 564 Ma (Higgins & van Breemen, 1998). The Rb content of plagioclase was determined by ICP-MS using a VG Plasma Quad PQ2 at the Royal Museum for Central Africa of Tervuren (Belgium) and was checked by LA-ICP-MS analyses at RSES (University of Canberra, Australia). A pulsed 193 nm ArF Excimer laser with 100 mJ output energy at a repetition rate of 5 Hz (Eggins *et al.*, 1998) was used and coupled to an Agilent HP7500 quadrupole ICP-MS system. Laser sampling was performed in a He–Ar atmosphere with a beam diameter of 150 μm. Analyses were calibrated using ^{29}Si as an internal standard isotope based on SiO_2 concentrations previously measured by XRF on plagioclase separates. NIST-612 glass was used as the external standard, assuming the composition given by Pearce *et al.* (1997).

Mineral modes

Mineral modes (Supplementary Dataset 1) were determined in a selection of cumulate samples using two independent methods: point counting and least-squares linear regression. Point counting was carried out on polished thin-sections from 210 samples. At least 1000 points were counted for each sample on a grid of 0·4 mm × 0·4 mm. The data obtained in volume per cent were converted to weight per cent using the density of the minerals calculated from their chemical composition. For samples where mineral compositions have not been determined, densities were calculated using mineral compositions obtained by interpolation from the adjacent samples. Mineral modes in weight per cent were also estimated using least-squares linear regression from the major element composition of the cumulus phases and whole-rocks (188 samples; Supplementary Dataset 7). The algorithms of Stormer & Nicholls (1978) were used for this regression. For samples where mineral analyses were not available, mineral compositions obtained by interpolation between adjacent samples were used. Sums of squares of the residuals ($\sum r^2$) are usually between zero and 0·5. Only seven samples have a $\sum r^2$ higher than 1·0. Both methods give consistent results.